

Investigating Spin Seebeck effect in various types of Hexaferrite

A Thesis

submitted to

Indian Institute of Science Education and Research Pune
in partial fulfillment of the requirements for the
BS-MS Dual Degree Programme

by

Robin K P



Indian Institute of Science Education and Research Pune
Dr. Homi Bhabha Road,
Pashan, Pune 411008, INDIA.

May, 2023

Supervisor: Dr. Sunil Nair

© Robin K P 2023

All rights reserved

Certificate

This is to certify that this dissertation entitled Investigating Spin Seebeck effect in various types of Hexaferrite towards the partial fulfilment of the BS-MS dual degree programme at the Indian Institute of Science Education and Research, Pune represents study/work carried out by Robin K P at Indian Institute of Science Education and Research under the supervision of Dr. Sunil Nair, Associate Professor, Department of Physics, during the academic year 2022-2023.



Dr. Sunil Nair

Committee:

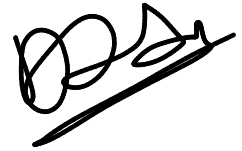
Dr. Sunil Nair

Dr. Mukul Kabir

This thesis is dedicated to my parents

Declaration

I hereby declare that the matter embodied in the report entitled Investigating Spin Seebeck effect in various types of Hexaferrite are the results of the work carried out by me at the Department of Physics, Indian Institute of Science Education and Research, Pune, under the supervision of Dr. Sunil Nair and the same has not been submitted elsewhere for any other degree.

A handwritten signature in black ink, consisting of several loops and a long horizontal stroke at the bottom.

Robin K P

Acknowledgments

I would like to express my heartfelt gratitude to everyone who has contributed to the successful completion of my project and supported me throughout my academic journey.

First and foremost, I am deeply indebted to my supervisor, Dr. Sunil Nair, for his continuous guidance and motivation. His unwavering faith in me and his support through all my challenges and gave me tremendous self belief and drive to keep working towards the progress of my project.

I would like to express my deep appreciation to my fellow researchers in the laboratory Anna, Murthy, Harshdip, Rohit, Vikram, Arun and Shruti, who have consistently encouraged and supported me throughout my work. Their unwavering willingness to address even my most trivial questions has been invaluable, and I will always be thankful for their guidance.

I would like to extend a special appreciation to Anna, who played an indispensable role in the completion of the project. Despite facing challenging circumstances, she dedicated herself to performing the sputtering and spin Seebeck measurements, without which the project would not have been possible. I am also indebted to Murthy for the Spin Seebeck measurements and valuable inputs for the thesis. I would also like to acknowledge Shruti for the dielectric measurements and insightful contributions to the project.

I would also like to extend my gratitude to the technical officers, Mr Anil and Mr Sudheer for their invaluable assistance in the operation of the FESEM facilities. I am also grateful to the staffs and members of other labs in h cross for their contribution in the successful completion of the project.

In addition, I express my gratitude to Dr. Mukul Kabir, my TAC member, whose insightful inputs and thought-provoking inquiries have challenged me to enhance my understanding of the subject matter. I appreciate his invaluable contribution to my research.

Last but not least, I would like to acknowledge my family and friends for their continual care and support throughout my life, particularly my parents for their unwavering faith in

my abilities. Their love and encouragement have been instrumental in my personal and academic growth, and I am deeply grateful to them forever.

Abstract

Spintronics is an emerging field of physics which deals with the spin degree of freedom of electron. It has the potential to be applied in future devices. Various discoveries were made which contributed to the growth of the field. One such discovery is the Spin Seebeck Effect (SSE) in 2008. Since then, SSE has been observed in conductors, semiconductors and insulators. In case of insulators, most of the studies were based on a class of compounds called garnets. Through this project, we aim to investigate the hexaferrites PbM ($\text{PbFe}_{12}\text{O}_{19}$), BaM ($\text{BaFe}_{12}\text{O}_{19}$) and BaY ($\text{Ba}_2\text{Zn}_2\text{Fe}_{12}\text{O}_{22}$) as a potential spintronics material. These compounds were prepared via solid state synthesis route and various measurements were conducted on them including Resistivity, Dielectric and Spin Seebeck Effect measurements. Comparison was made amongst them to study the effect of changing the composition.

Contents

| | |
|---|-----------|
| Abstract | xi |
| 1 Introduction | 1 |
| 1.1 Introduction | 1 |
| 1.2 Spin Current | 2 |
| 1.3 Spin Hall Effect (SHE) and Inverse SHE (ISHE) | 4 |
| 1.4 Seebeck effect | 6 |
| 1.5 Spin Seebeck Effect (SSE) | 7 |
| 1.6 Nernst effect and Anomalous Nernst effect (ANE) | 9 |
| 1.7 Hexaferrites | 9 |
| 1.8 Crystal Structure | 11 |
| 2 Experimental Techniques | 17 |
| 2.1 Synthesis | 17 |
| 2.2 X Ray Diffraction (XRD) | 20 |
| 2.3 Structural Analysis | 21 |
| 2.4 Field Emission Scanning Electron (FE SEM) and Energy Dispersion X ray (EDX) | 24 |
| 2.5 Leaching | 25 |

| | | |
|----------|---|-----------|
| 2.6 | Magnetron sputtering | 25 |
| 2.7 | Atomic Force Microscope (AFM) | 26 |
| 2.8 | Dielectric measurements | 27 |
| 2.9 | Spin Seebeck Measurement | 28 |
| 2.10 | Resistivity measurements | 30 |
| 3 | Results and Discussion | 33 |
| 3.1 | Synthesis and XRD analysis | 33 |
| 3.2 | Structural Refinement | 38 |
| 3.3 | Resistivity measurements | 44 |
| 3.4 | Dielectric measurements | 47 |
| 3.5 | Surface morphology of slabs | 50 |
| 3.6 | Spin Seebeck Measurements | 51 |
| 4 | Conclusion and future works | 59 |

List of Figures

| | | |
|------|---|----|
| 1.1 | Illustration of (a) unpolarized current, (b) spin-polarized current, (c) fully polarized current, and (d) pure spin current. [15] | 3 |
| 1.2 | Illustration of 1-D spin waves in YIG [11] | 3 |
| 1.3 | Illustrating the difference between a)Normal Hall effect b)Anomalous Hall effect c)Spin Hall effect [10] | 5 |
| 1.4 | Illustrating the scattering of electrons in SHE [1] | 5 |
| 1.5 | Illustrating the scattering of electrons in ISHE [1] | 6 |
| 1.6 | Illustration of a thermocouple used to demonstrate Seebeck effect. The voltage across the terminal is proportional to the temperature difference between the ends. [57] | 7 |
| 1.7 | Schematic of the experimental setup for the longitudinal spin Seebeck effect[31] | 7 |
| 1.8 | Structure of S block. The top layer is one layer of R block [37] | 11 |
| 1.9 | Structure of R block [37] | 12 |
| 1.10 | Structure of T block [37] | 13 |
| 1.11 | Crystal structure of one unit cell of M type [27] | 14 |
| 1.12 | Crystal structure of one unit cell of Y type [33] | 15 |
| 2.1 | Crucible arrangement for sintering pellet. The pellet is kept in a small crucible, sprinkled with a little PbO and covered with a lid and this in turn is kept inside a bigger crucible which is also covered by a lid. | 18 |
| 2.2 | Schematic diagram representing Bragg's Law. [63] | 21 |

| | | |
|------|---|----|
| 2.3 | Schematic diagram of scanning electron microscope [30]. | 24 |
| 2.4 | Schematic diagram showing the working of a DC Magnetron sputtering system [2]. | 25 |
| 2.5 | Working of atomic force microscope [62]. | 26 |
| 2.6 | Platinum deposited on sapphire substrate under AFM. The thickness was measure to be roughly 40 nm. | 27 |
| 2.7 | (a) Platinum deposited on BaY with gold wire attached to the sample using silver paste. (b) Image of the sample holder | 29 |
| 3.1 | XRD data of $\text{PbFe}_{12}\text{O}_{19}$ before and after leaching | 35 |
| 3.2 | FE SEM images after leaching. We can see grains of the sample along with a lot of impurities | 35 |
| 3.3 | FE SEM images after leaching. Compared to the images before leaching, no impuriteis seem to present along with the grains. | 35 |
| 3.4 | XRD data of $\text{Ba}_2\text{Zn}_2\text{Fe}_{12}\text{O}_{22}$ compared to the reference data. No extra peaks were observed. | 37 |
| 3.5 | FE SEM images of BaY and the size of individual grains | 37 |
| 3.6 | XRD data of $\text{BaFe}_{12}\text{O}_{19}$ compared to the reference data. No extra peaks were observed. The intensity of some peaks do not match which can be attributed to the preferred orientation of the grains | 38 |
| 3.7 | FE SEM images of BaM and the size of individual grains | 38 |
| 3.8 | Rietveld refinement plot for PbM | 39 |
| 3.9 | Rietveld refinement plot for BaY | 41 |
| 3.10 | Rietveld refinement plot for BaM | 43 |
| 3.11 | Plot of resistivity vs temperature while cooling and warming the BaM sample | 45 |
| 3.12 | Arrhenius fitting was done at high temperature. $\ln(\rho)$ vs $1/T$ was plotted for BaM | 45 |
| 3.13 | Mott fitting was done at low temperature. $\ln(\rho)$ vs $1/T^4$ was plotted for BaM | 46 |

| | |
|---|----|
| 3.14 (a) Real part of dielectric constant of BaM vs temperature for various frequencies (b) Imaginary part of dielectric constant of BaM vs temperature for various frequencies | 47 |
| 3.15 Dielectric loss of BaM vs temperature for various frequencies | 48 |
| 3.16 (a) Real part of dielectric constant of PbM vs temperature for various frequencies (b) Imaginary part of dielectric constant of PbM vs temperature for various frequencies | 48 |
| 3.17 Dielectric loss of PbM vs temperature for various frequencies | 49 |
| 3.18 Surface of well polished slabs under AFM. The roughness of the respective area is given in the bracket (a) BaM (585 nm) (b) BaY (266 nm) (c) PbM (194 nm) | 50 |
| 3.19 Resistance of platinum deposited on top as a function of temperature | 52 |
| 3.20 Spin Seebeck signal as a function of thermal gradient | 53 |
| 3.21 Spin Seebeck signal as a function of magnetic field | 53 |
| 3.22 Spin Seebeck signal as a function of temperature | 54 |
| 3.23 Resistance of platinum deposited on top as a function of temperature | 55 |
| 3.24 Spin Seebeck signal as a function of thermal gradient | 55 |
| 3.25 Spin Seebeck signal as a function of magnetic field | 56 |
| 3.26 Spin Seebeck signal as a function of temperature | 56 |

List of Tables

| | | |
|-----|---|----|
| 1.1 | Types of hexaferrite and their chemical composition along with their transition temperature | 10 |
| 1.2 | Types of hexaferrite and their corresponding stacking order of S, R, T blocks to form the structure | 13 |
| 2.1 | Parameters for synthesis of $\text{PbFe}_{12}\text{O}_{19}$ | 19 |
| 2.2 | Parameters for synthesis of $\text{Ba}_2\text{Zn}_2\text{Fe}_{12}\text{O}_{22}$ | 20 |
| 2.3 | Parameters for synthesis of $\text{BaFe}_{12}\text{O}_{19}$ | 20 |
| 3.1 | Table demonstrating the change in atomic ratio of Pb : Fe before and after leaching | 36 |
| 3.2 | Refined lattice and fitting parameters for $\text{PbFe}_{12}\text{O}_{19}$ | 40 |
| 3.3 | Refined atomic positions and site occupancy | 40 |
| 3.4 | Refined lattice and fitting parameters for $\text{Ba}_2\text{Zn}_2\text{Fe}_{12}\text{O}_{22}$ | 41 |
| 3.5 | Refined atomic positions and site occupancy | 42 |
| 3.6 | Refined lattice and fitting parameters for $\text{BaFe}_{12}\text{O}_{19}$ | 43 |
| 3.7 | Refined atomic positions and site occupancy | 44 |
| 3.8 | Fitting parameters and the corresponding physical values | 46 |

Chapter 1

Introduction

1.1 Introduction

Currently, the utilization of the spin degree of freedom of electrons is limited to storage devices. However, there has been a recent trend in exploiting the spin of electrons for other purposes such as transmitting information. Traditionally, devices relied on the charge of electrons and holes to relay information, but a new technology called Spintronics has emerged, which employs the spin degree of freedom of electrons to accomplish the same tasks and more. Spintronics provides several advantages over the conventional methods, including reduced power consumption by eliminating Joule heating, zero standby leakage current, and the ability to scale down devices to the nano size, making them more portable. Spintronic devices operate using spin current rather than charge current. The field of spintronics owes its inception to the discovery of GMR (Giant Magnetoresistance) in 1988 [7]. Other discoveries that have driven the growth of the field include TMR (Tunnel Magnetoresistance)[67], STT (Spin Transfer Torque)[54], and SHE (Spin Hall effect)[52].

Currently, the primary obstacles in the field of spintronics are related to creating, manipulating, and detecting spin currents. A growing subfield of spintronics, known as spin caloritronics, focuses on the interplay between spin, charge, and heat currents. The spin Seebeck effect (SSE) is the phenomena in which spin current and spin voltage is generated by placing a magnetic material in a temperature gradient. This project focuses on investigating SSE in a class of compounds called Hexaferrites.

There are a number of magnetic insulators like spinels, garnets, hexaferrites etc. Usually spinels and garnets are classified as soft magnetic materials while hexaferrites are classified as hard.[21] A number of works have been published on Spin Seebeck effect on soft magnetic materials [58] but only limited ones in hard magnetic materials. Studies have been conducted on SSE in hexaferrites in both thin films and bulk materials, but most of them with Ba or Sr as the large divalent cation. The project also aims to look into the effect which Pb has when substituted for the large divalent cation. Before understanding Spin Seebeck Effect, a number of terms and phenomena that has to be elaborated.

1.2 Spin Current

Just like conventional current is a flow of charges, spin current is the flow of spin angular momentum of electrons. A lot of debates are going on regarding the proper definition of spin current. A definition of spin current is provided as follows [1]

$$J_s = \sum_k s_k^z v_k \quad (1.1)$$

where s_k^z is the component of spin density s_k along the z axis, which we choose as the axis of quantization. v_k is the velocity of excitations associated with the spin density s_k . k represents the momentum Now there are two mediators of the spin current (1) conduction electron (2) magnon.

In a conductor, when the electrons with their spin oriented along one direction, say up move in one direction and the electrons with the opposite spin orientation (down) move in the opposite direction to that of spin up, then there won't be any net flow of charges but there will be a flow of angular momentum. This constitutes the case of a pure spin current.

For the conduction electron pure spin current, the z component of the spin density is given by

$$s_k^z = c_{k,\uparrow}^\dagger c_{k,\uparrow} - c_{k,\downarrow}^\dagger c_{k,\downarrow} \quad (1.2)$$

where $c_{k,\uparrow}^\dagger$ and $c_{k,\downarrow}^\dagger$ are the creation operators for conduction electrons with projection of spin along up and down the z axis respectively.

Therefore, the expectation value of pure spin current mediated by electrons (J_s^{c-el}) is calcu-

lated by taking the statistical average,

$$J_s^{c-el} = \sum_k v_k (\langle c_{k,\uparrow}^\dagger c_{k,\uparrow} \rangle - \langle c_{k,\downarrow}^\dagger c_{k,\downarrow} \rangle) \quad (1.3)$$

where v_k is the velocity of the conduction electrons.

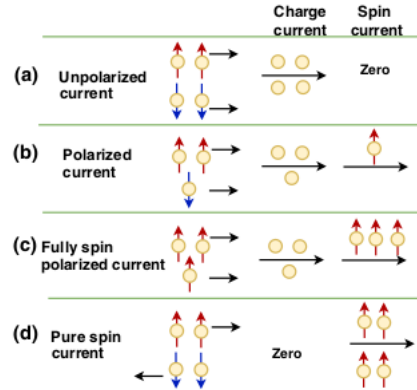


Figure 1.1: Illustration of (a) unpolarized current, (b) spin-polarized current, (c) fully polarized current, and (d) pure spin current. [15]

Initially, it was believed that the conduction electrons are the only carrier of spin current. However, subsequent experiments demonstrated that spin currents can also be generated and transmitted in insulators [59]. This discovery led researchers to propose a new carrier of spin current, known as spin waves. Spin waves are excitations or oscillations in relative arrangement of magnetic moments in a magnetic material [12]. The quasi particle of this excitation are called as magnons much like phonons are excitations of lattice vibration. This spin waves are observed both in conductors as well as insulators.

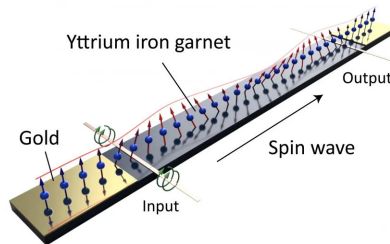


Figure 1.2: Illustration of 1-D spin waves in YIG [11]

The z component of its spin density is given by

$$s_k^z = S_0 - b_k^\dagger b_k \quad (1.4)$$

where b_k^\dagger is the creation operator for magnons with momentum k .

Taking the expectation value of magnon pure spin current J_s^{mag} is given by

$$J_s^{mag} = -\frac{1}{2} \sum_k v_k (\langle b_k^\dagger b_k \rangle - \langle b_{-k}^\dagger b_{-k} \rangle) \quad (1.5)$$

where v_k is the magnon velocity. So we can use the relation $v_{-k} = v_k$ to cancel out the term S_0 . Here k is the momentum and it takes non negative values.

Spin diffusion length is the length over which the spin currents generated actually persists. In the spin current mediated by the conduction electrons, the spin diffusion length is in the range of nanometers, ranging from tens of nanometers to hundreds of nanometers [25]. For the case of magnon mediated spin current, the spin diffusion length can be in the range of micrometers to millimeters [59]. Unlike charge current, in which the total charge of the electrons are conserved, the total spins of the electrons is not conserved. This is due to the spin orbital coupling which converts the spin of electron to the orbital angular momentum and vice versa [48].

There are various techniques to generate and detect these spin currents. In conductors, one prominent method to generate conduction mediated spin current is by the process of Spin Hall Effect and Inverse Spin Hall Effect. In magnetic insulators and conductors, spin waves can be generated by the process of Spin Seebeck Effect. As these are the processes used in the project, the main focus will be on these methods of generating spin current. Other methods of generating spin current include using light, electric field, magnetic field, circularly polarized photoexcitation etc [21].

1.3 Spin Hall Effect (SHE) and Inverse SHE (ISHE)

When a charge current passes through a conductor, a spin current is developed transverse to the charge current. It happens due to the spin orbital coupling in which electrons are scattered off the scattering sites depending on the spin of the electrons. The electrons with opposite spins are scattered off in opposite direction thus constituting a spin current. [14] [22]

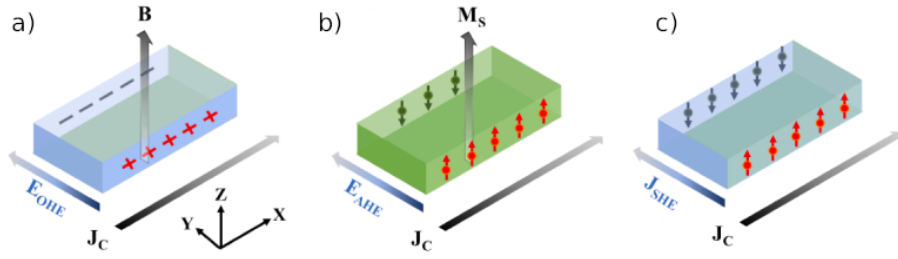


Figure 1.3: Illustrating the difference between a) Normal Hall effect b) Anomalous Hall effect c) Spin Hall effect [10]

The spin current generated is proportional to the charge current and its direction is given by the equation

$$\vec{J}_s \propto \theta_H \frac{2e}{\hbar} \hat{\sigma} \times \vec{J}_c \quad (1.6)$$

Where θ_H is the spin Hall angle, $\hat{\sigma}$ denotes the direction of spin polarization, \vec{J}_c represents the direction of flow of electrons.

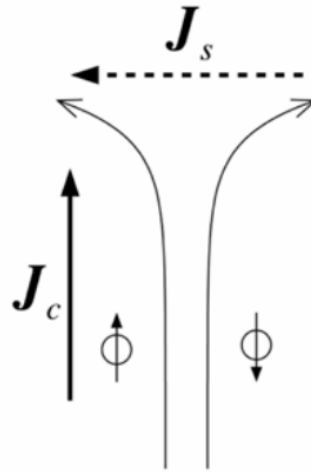


Figure 1.4: Illustrating the scattering of electrons in SHE [1]

Inverse Spin Hall effect is the exact opposite process in which a spin current is converted to charge current. In this case, since the electrons with opposite spins are moving in opposite

direction, they are both scattered off in the same direction. This is the technique used to detect the spin current in our experiment. It is given by

$$\vec{J}_c \propto \theta_H \frac{2e}{\hbar} \hat{\sigma} \times \vec{J}_s \quad (1.7)$$

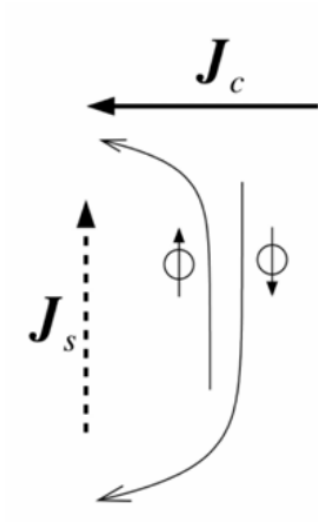


Figure 1.5: Illustrating the scattering of electrons in ISHE [1]

This happens mostly in heavy metals that has a high spin orbital coupling which facilitates easy conversion of spin current to charge current and vice versa. There are various mechanisms by which this happens and the origin of all them lies in the spin orbital coupling [24].

1.4 Seebeck effect

When a temperature gradient is applied across two points in a conductor, an electromotive force is induced in the conductor between those two points. Electrons located at the hotter end possess greater kinetic energy in contrast to those located at the colder end, leading to a higher degree of diffusion among the hotter electrons compared to their colder counterparts. So averaging out would cause a directional flow of electrons from the hotter end to the colder end. [4]. The emf generated is directly proportional to the temperature difference

and inversely proportional to the distance between the two points. The Seebeck effect is quantified by a coefficient called Seebeck Coefficient (S), which is defined as the ratio of the voltage induced divided by the thermal gradient.

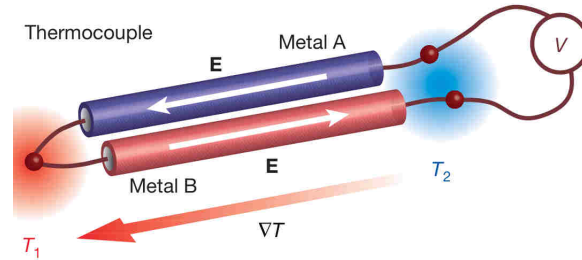


Figure 1.6: Illustration of a thermocouple used to demonstrate Seebeck effect. The voltage across the terminal is proportional to the temperature difference between the ends. [57]

1.5 Spin Seebeck Effect (SSE)

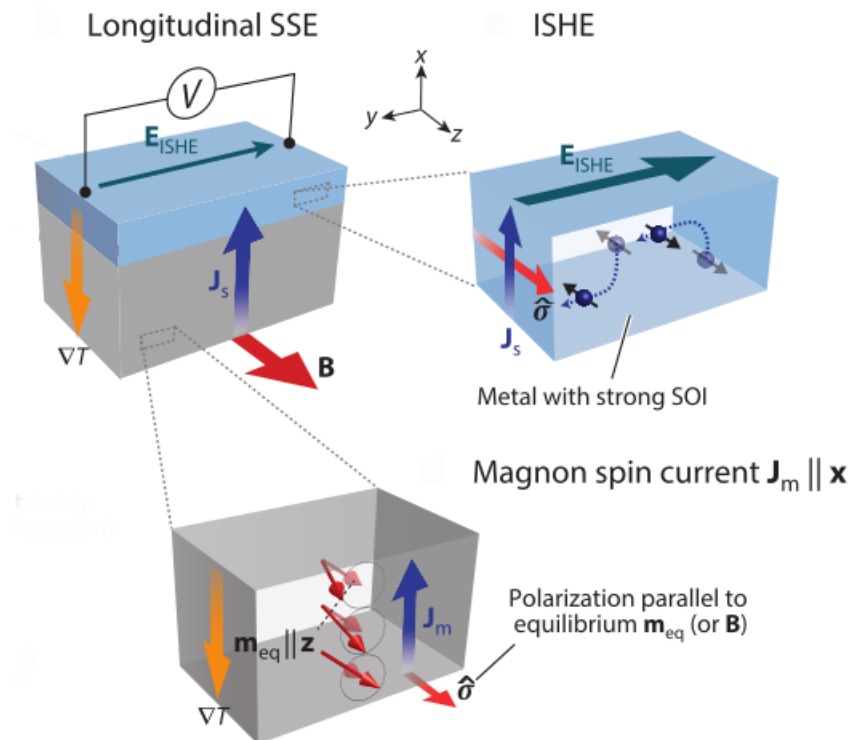


Figure 1.7: Schematic of the experimental setup for the longitudinal spin Seebeck effect[31]

When a magnetic material is placed under the influence of a temperature gradient, a spin current is generated and propagated along the thermal gradient and is injected from the magnetic material into an attached nonmagnetic metal [1]. It was first discovered in conductors and subsequently in semiconductors and later insulators. This occurs at macroscopic length scales of the order of millimeters suggesting that conduction electrons are not sufficient to explain the phenomena and magnons play a huge role in the propagation of spin currents. There are two configurations used to measure Spin Seebeck effect (1) transverse and (2) longitudinal spin Seebeck effect and they are as given in the figure (1.7). Earlier, people used to measure the transverse SSE but nowadays focus has been shifted to longitudinal SSE. [1] Figure 1.7(a) shows the schematic of a device used to measure longitudinal SSE. The magnetic material is shaped in the form of a slab and a non magnetic material with high spin orbital coupling like platinum is sputtered on top of it. A temperature gradient ∇T is applied along the z direction perpendicular to non magnetic material interface. The sample end is maintained at a higher temperature than the non magnetic end. A magnetic field is applied perpendicular to the temperature gradient along the x direction. The temperature gradient results in net propagation of magnons from the hot end to the cold end. Once they reach the interface, the spin current is injected from the magnetic material to non magnetic material by the process of spin pumping. The injected spin current is given by the equation [64]

$$j_s \approx \frac{\gamma \hbar K_B}{2\pi M_s V_a} \frac{g_r}{A} (T_m - T_e) \quad (1.8)$$

where γ is the gyro magnetic ratio of electron, K_B is the Boltzmann constant, M_s is the saturation magnetisation, V_a is the coherence volume, g_r is the real part of spin mixing conductance and A is the area of the interface. T_m and T_e denotes the effective temperature of the magnons in magnetic material and effective temperature of conduction electrons in non magnetic material respectively. In the non magnetic material, the spin current is converted to charge current by ISHE, which will be along the y direction as per the equation 1.7. The voltage generated across the non magnetic layer is given by [46]

$$V_{obs} = R_N w \lambda_N \frac{2e}{\hbar} \theta_H \left[\tanh\left(\frac{t_N}{2\lambda_N}\right) \right] j_s \quad (1.9)$$

where R_N is the resistance of the platinum on top, w is the width of the platinum layer, λ_N is the spin diffusion length on conduction electrons in the platinum, θ_H is the spin hall angle of platinum, t_N is the thickness of the platinum layer

The voltage obtained across the platinum is normalised by the equation given by

$$V_{LSSSE} = \frac{V_{obs}t}{R_N\Delta Tl} \quad (1.10)$$

where t is the thickness of the magnetic material, R_N is the resistance across the platinum layer at the given temperature, Δ is the temperature gradient applied across the multilayer and l is the distance between the contacts in the platinum layer.

Under thermal equilibrium condition, spin currents flow from the magnetic material to non magnetic material and vice versa but they will be equal in magnitude. But when there is a thermal non equilibrium, more spin current flow from one side to the other.

1.6 Nernst effect and Anomalous Nernst effect (ANE)

When a magnetic field is applied perpendicular to the temperature gradient across a conductor, the emf would be generated perpendicular to both the magnetic field and the temperature gradient. This is called as Nernst effect. It arises due to Lorentz force acting on electrons when they move through the magnetic field.

Anomalous Nernst Effect (ANE) is when an emf is generated perpendicular to mutually orthogonal temperature gradient and internal magnetization. [10]

One challenge while measuring Spin Seebeck signal is that ANE signal can come as parasitic signal along with the SSE signal. So, it becomes important to separate or eliminate ANE signal altogether. There are many ways to do this. One of the ways to do this by choosing a material which doesn't have any conduction electrons. So it is essential to select a material which has high resistance. Hexaferrites are a class of material which usually has a high value of resistance, which is one of the reasons they were chosen for the studies.

1.7 Hexaferrites

They are compounds containing iron oxides with a general formula $a \text{ BaO} \cdot b \text{ MeO} \cdot c \text{ Fe}_2\text{O}_3$, where a, b, c are whole numbers, Me is a small divalent metal and Ba can be replaced by other large divalent metals like Sr , Pb , Ca , etc. They are mostly ferrimagnets and all of them are found to have a hexagonal crystal structure, with 2 crystalline lattice parameters 'a' and 'c'.

'a' is the width of the hexagonal plane of the unit cell and 'c' is the height of the unit cell. When placed in a magnetic field, in most cases, the preferred direction of magnetisation is along the c axis. They are called as uniaxial hexaferrites. But in some cases, especially in the ones containing Co as Me, the preferred direction can be in a plane perpendicular to c axis or in a cone, and they are called as hexaplana ferrites. The magnetization can rotate without difficulty throughout 360° within the plane or cone, however, the high magnetic anisotropy energy locks the magnetization within this plane or cone [43].

The interesting property that makes hexaferrites different from other magnetic insulators is the high anisotropy. This gives it a high remanent and coercive field which leads to manifestation of SSE without application of an external magnetic field. This has potential applications in areas which deal with conversion of heat and light into electricity. [34]. The high resistivity of the order of $10^8 \Omega \text{ cm}$ [43] enables us to measure the spin Seebeck signal without the interference of Anomalous Nernst signal.

The simplest of the hexaferrites is called M type, which is obtained by setting $a=1$ $b=0$ and $c=6$ in the general formula giving the overall formula as $\text{BaFe}_{12}\text{O}_{19}$, often written as BaM. The space group of it is $P63/mmc$. Other types of hexaferrites are obtained by putting in different values for a,b and c. These are generally synthesised by heating a well mixed sample of raw materials and at different temperatures, where each hexaferrite peak at different temperature range. Some of the other hexaferrites are as given below.

| a | b | c | Formula | Type | Transition Temperature ($^\circ\text{C}$) |
|----------|----------|----------|---|-------------|---|
| 1 | 0 | 6 | $\text{BaFe}_{12}\text{O}_{19}$ | M type | 450 |
| 2 | 2 | 6 | $\text{Ba}_2\text{Me}_2\text{Fe}_{12}\text{O}_{22}$ | Y type | 340 |
| 3 | 2 | 12 | $\text{Ba}_3\text{Me}_2\text{Fe}_{24}\text{O}_{41}$ | Z type | 410 |
| 1 | 2 | 8 | $\text{BaMe}_2\text{Fe}_{16}\text{O}_{27}$ | W type | 490 |
| 2 | 2 | 14 | $\text{Ba}_2\text{Me}_2\text{Fe}_{28}\text{O}_{46}$ | X type | 470 |
| 4 | 2 | 18 | $\text{Ba}_4\text{Me}_2\text{Fe}_{36}\text{O}_{60}$ | U type | 430 |

Table 1.1: Types of hexaferrite and their chemical composition along with their transition temperature

1.8 Crystal Structure

The large oxygen atoms form the crystal structure and the large divalent cation, Ba^{2+} replacing oxygen ions in the oxygen lattice structure. As Ba^{2+} ion is slightly smaller than O^{2-} ion, it distorts the lattice structure locally. The smaller divalent cation and Fe^{3+} cation occupies the tetrahedral, octahedral and trigonal bipyramidal sites in the oxygen framework.

One way to look at the structure is being composed of basic building blocks called S,R and T blocks.

(1) S block – The S block is made up of two spinel units and therefore has the unit formula $\text{Me}_2\text{Fe}_4\text{O}_8$, where Me can be either divalent or trivalent metal. Each S block contains two layers of four oxygen atoms. Between the 2 oxygen layers, there are interstitial sites, 2 tetrahedral and one octahedral, which are occupied by the small cations. Now between the oxygen layer of S block and oxygen layer of the next block lies 3 octahedral sites filled in by the cations. Therefore in total, 6 cations are associated with one S block. These octahedral and tetrahedral sites have opposing spins due to super exchange, thus giving a net total of two moments for the S block [43].

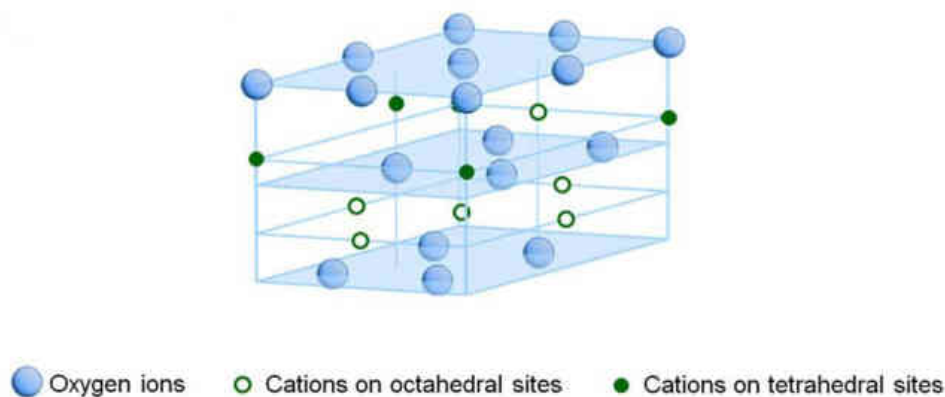


Figure 1.8: Structure of S block. The top layer is one layer of R block [37]

(2) R block – The R block made up of three hexagonally packed layers of four oxygen atoms each, however, in the central layer, a barium ion of comparable size replaces one of the oxygen atoms to give the unit formula $\text{BaFe}_6\text{O}_{11}$. The large size of the Ba ion creates a distortion in the lattice structure, which leads to changes in the shape of the interstitial sites. Between the outer layer and central layer of oxygen, lies an octahedral site, which would

have been a tetrahedral site if it were not for the distorting Ba atom. As there are 2 layers on either side of the central layer, it results in 2 octahedral sites between the layers. There is one octahedral site within the central layer, which is distorted to trigonal bipyramidal due to the Ba atom. Now between the outer layer and the adjacent block, there are 3 true octahedral sites. In total, there are 5 octahedral sites and one trigonal bipyramidal site. The spin of atom at these sites retains that of the undistorted one, resulting in a net spin of 2 moments for the R block [43].

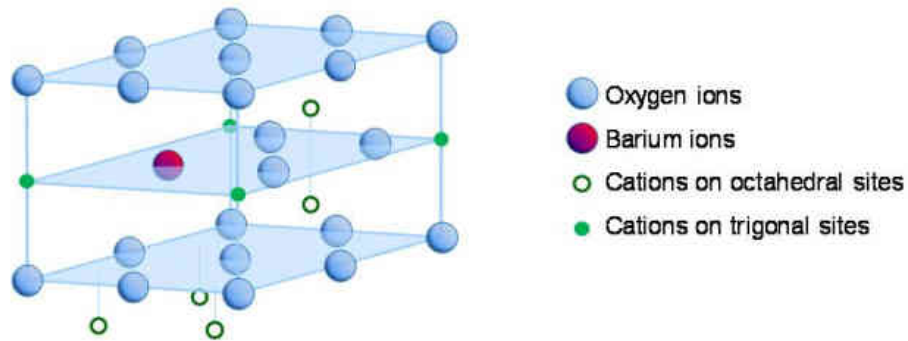


Figure 1.9: Structure of R block [37]

(3) T block – The T block consists of four oxygen layers, with a barium atom replacing an oxygen atom in the two layers in the middle, which gives the unit formula $Ba_2Fe_8O_{14}$. As there are two sizeable barium ions located opposite each other in adjacent layers, the cations that would have occupied the five-coordinate sites are displaced in opposite directions alongside the barium ions. This reduces the trigonal bipyramidal sites to tetrahedral sites, resulting in two tetrahedral and six octahedral sites. Out of the six octahedral moments, 2 of them are aligned along the two tetrahedral moments, thus giving a net moment of zero for the T block [43].

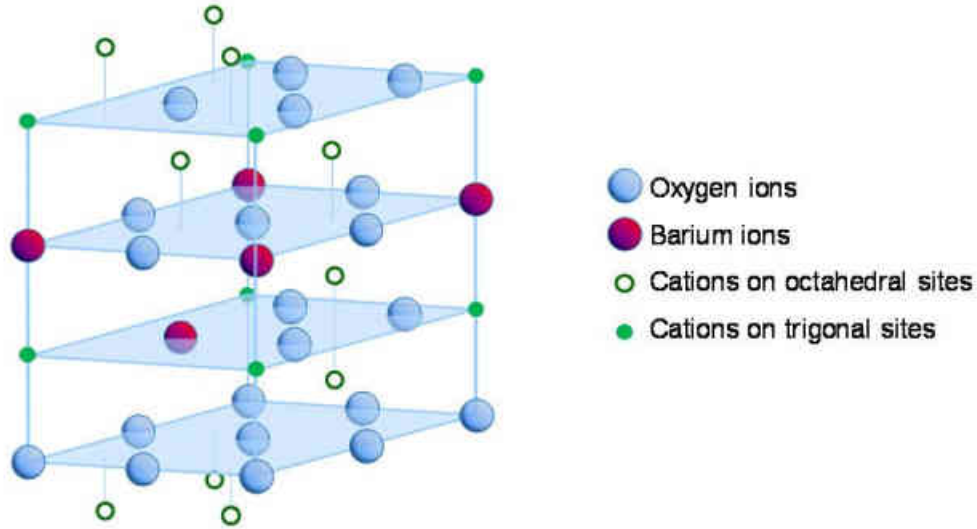


Figure 1.10: Structure of T block [37]

These 3 block when placed on top of each other in stacks give rise to all hexaferrites and the arrangement needed to produce each type is given below. Multiples of molecular units constitute the unit cell for most of the hexaferrites, two molecular units for M, W and Z ferrite, and three molecular units for X and Y ferrite, but only one molecular unit for U ferrite.

| Ferrite | Formula | Stacking Order |
|---------|---|----------------|
| M | $\text{BaFe}_{12}\text{O}_{19}$ | SRS*R* |
| Y | $\text{Ba}_2\text{Me}_2\text{Fe}_{12}\text{O}_{22}$ | 3(ST) |
| Z | $\text{Ba}_3\text{Me}_2\text{Fe}_{24}\text{O}_{41}$ | STSRS*T*S*R* |
| W | $\text{BaMe}_2\text{Fe}_{16}\text{O}_{27}$ | SSRS*S*R* |
| X | $\text{Ba}_2\text{Me}_2\text{Fe}_{28}\text{O}_{46}$ | 3(SRS*S*R*) |
| U | $\text{Ba}_4\text{Me}_2\text{Fe}_{36}\text{O}_{60}$ | SRS*R*S*T |

Table 1.2: Types of hexaferrite and their corresponding stacking order of S, R, T blocks to form the structure

1.8.1 M type

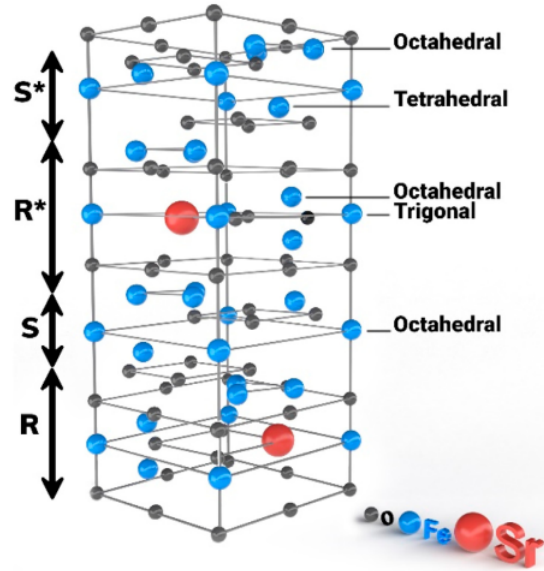


Figure 1.11: Crystal structure of one unit cell of M type [27]

As we can see, the unit cell of M type consists of S, R, S*, R* blocks stacked on top of each other. It belongs to Hexagonal lattice structure with a space group of P63/mmc. The lattice parameters of BaM are $c = 23.183 \text{ \AA}$ and $a = b = 5.8920 \text{ \AA}$ [39]. The ratio of height to width is 3.94, so BaM has a large crystalline anisotropy, which becomes even higher for the other hexagonal ferrites. SrM has smaller lattice constants due to the smaller size of the Sr^{2+} ion, giving the parameters $c = 23.03 \text{ \AA}$ and $a = b = 5.86 \text{ \AA}$. Otherwise it has the same structure and unit cell ordering as BaM [5]. The Pb^{2+} ion is also smaller than Ba^{2+} , and the lattice parameters for PbM are $c = 23.106 \text{ \AA}$, $a = b = 5.894 \text{ \AA}$ [40].

In BaM, all the cations are Fe^{3+} , and as they are in high spin state, gives a magnetic moment of $5\mu_B$ along the c axis for each cation. This gives the M type a theoretical magnetic moment of $20\mu_B$ for a single unit cell and this gives it a high saturation magnetisation of $72 \text{ A m}^2\text{kg}^{-1}$, T_c of 450°C . Theoretical maximum coercivity is 594 kA m^{-1} but the reported values are around $159\text{-}255 \text{ kA m}^{-1}$ [43].

1.8.2 Y type

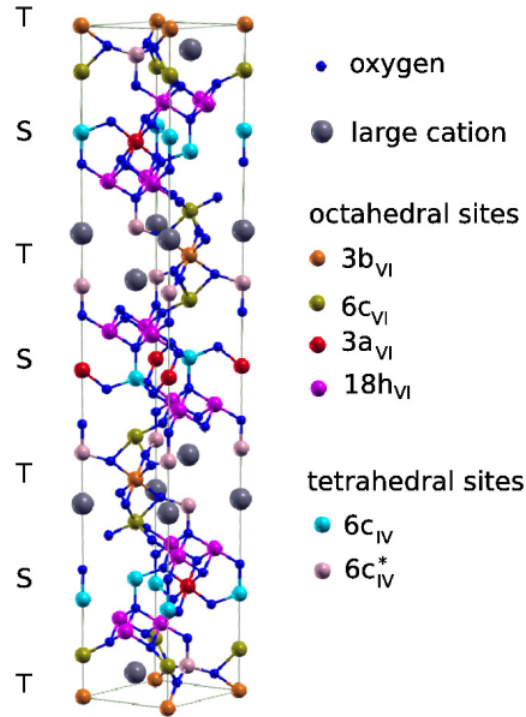


Figure 1.12: Crystal structure of one unit cell of Y type [33]

The Y type is formed from S and T blocks and doesn't contain R block. Each unit cell is composed of 3 molecular units. They belong to trigonal crystal system with a space group of $R\bar{3}m$. $Ba_2Zn_2Fe_{12}O_{22}$ was found to have lattice parameters of $a = b = 5.8763 \text{ \AA}$ and $c = 43.566 \text{ \AA}$ [49]. All the Y type hexaferrites are hexaplana ferrites, which means that their easy axis of magnetization is along the ab plane [23]. In case of $Ba_2Zn_2Fe_{12}O_{22}$, Fe atoms are in high spin state and each Fe atom contributes $5\mu_B$ to the unit cell. The Zn atoms being non magnetic doesn't contribute to the magnetic moment. The Zn atoms always occupy the tetrahedral sites [6]. For each unit cell, 12 tetrahedral positions are available and Zn occupies 6 out of the 12 available positions. The rest of the tetrahedral positions are filled in by the Fe atoms. In a unit cell, there are 30 octahedral positions, all of which are occupied by Fe atoms. Due to super exchange, the moment of tetrahedral opposes that of octahedral. One thing to keep in mind is that this empirical rule cannot be directly used in our case as the distortion due to barium changes the original geometry. So, it has to be applied

to the original geometry without distortion. This would result in 24 out of 30 octahedral sites having same spin orientation while the rest 6 octahedral and 12 tetrahedral having the opposite spin orientation. Since out of the 12 tetrahedral sites, 6 are occupied by non magnetic Zn atom, they won't contribute to the magnetism. So the net magnetic spin of a single unit cell will be $24 - (6 + 6)$, which would be 12, which give the unit cell a net theoretical magnetic moment of $60 \mu_B$.

The reported values of saturation magnetisation at room temperature is $42 \text{ A m}^2\text{kg}^{-1}$, while the Curie temperature is reported to be 130°C [43].

Chapter 2

Experimental Techniques

2.1 Synthesis

The reactions were carried out using Solid State synthesis and Coprecipitation methods. For solid state synthesis, metal oxides in the form of powder were carefully weighed out to match for the stoichiometry of the final sample. They were then mixed thoroughly in an agate mortar and pestle for around 2-3 hours. This breaks down the size of the powder particles and ensure homogeneous mixing of the raw materials. The reactant mixture was then pelletized using a Kbr press in order to increase the area of contact between the grains, which ensures easy diffusion of the atoms across the grain during the process of sintering [61]. As the diffusion is a slow process, high temperatures and long sintering times are required for solid state reactions [53]. Sintering was carried out using PID controlled programmable furnaces, which allows us to fine tune the sintering parameters. Sintering atmosphere is also an important parameter especially in our case.

One of the raw materials we are working with is PbO, has a melting point of 888 °C [41] and a boiling point of 1470 °C [42]. Despite having a boiling point well above the sintering temperatures, it sublimates at around 800°C [32]. This results in a loss of PbO from the sintering pellet, thus changing the stoichiometry of the reactants. To overcome this problem, the pellets were kept in a PbO rich atmosphere. This was made possible with the help of double crucible setup with some PbO sprinkled around the pellet, as seen in the figure 2.1. When the temperature rises, the sprinkled PbO vaporizes, but the lids ensure that it does

not leak out of the crucibles. This increases the partial pressure of PbO inside the crucible, which in turn prevents further sublimation of PbO [13]. This was required only when lead compounds were used as a raw material.

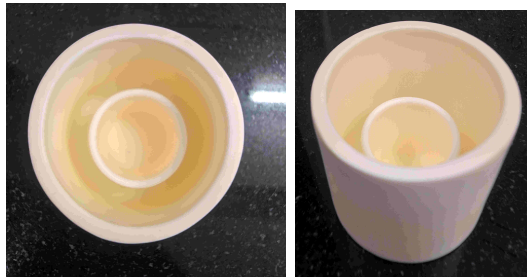


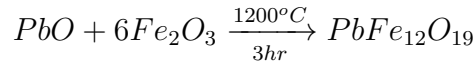
Figure 2.1: Crucible arrangement for sintering pellet. The pellet is kept in a small crucible, sprinkled with a little PbO and covered with a lid and this in turn is kept inside a bigger crucible which is also covered by a lid.

Solid state synthesis is a fairly simple method and the main advantage is that the raw materials remain in powder form without the need to find a suitable solvent to dissolve the raw materials. But the main limitation is that higher sintering temperature and longer sintering times are required. This limitation is notable when volatile substances are used, along with higher sintering temperatures. Even the double crucible setup may not be sufficient to guarantee the proper occurrence of the reaction. In such cases, one of the strategies is to bring down the temperature range at which the reaction happens. One of the ways for achieving this is to employ a different method of mixing like Co-precipitation [50].

Co-precipitation involves mixing the raw materials in a liquid form, which results in its mixing uniformly to the ionic range. As the individual ions are now in contact with each other, a smaller temperature and time are required for the diffusion and rearrangement of atoms [19]. The raw materials were weighed to match for the stoichiometry of the final sample and they were put into a beaker containing a solvent and mixed well using magnetic stirrer such that all the raw materials dissolve. Care has to be taken while choosing the raw materials such that they all have to be soluble in a particular solvent. To this solution, NaOH is added which results in the precipitation of the salts in hydroxide form. The precipitate was then filtered out using filtering paper and then dried using IR lamp. The dried out residue was then crushed into fine powder using an agate mortar and pestle, following which pellets were made and sintered just as in the solid state synthesis [35].

2.1.1 Synthesis of $\text{PbFe}_{12}\text{O}_{19}$

Synthesis of $\text{PbFe}_{12}\text{O}_{19}$ was carried out using solid state synthesis. The raw materials used were PbO (Alfa Aesar, 99.9%) and Fe_2O_3 (Sigma Aldrich, 99%), in the molar ratio 1:6 respectively, with the total weight of raw materials being around 1.2 grams. They were mixed using agate mortar and pestle for 2.5 hours, following which it was pelletized. The pellets obtained were sintered at 1200°C for 3 hours, in a PbO rich atmosphere, with the help of alumina crucibles. The sintering was carried out in P310 Nabertherm furnace. The sintering temperature was achieved with a ramping rate of $6.44^\circ/\text{min}$. The balanced reaction equation is as given below.

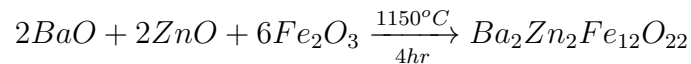


| Heating Rate | Temperature | Time | Environment |
|-------------------------------|-----------------------|------|-------------------|
| 5 $^\circ\text{C}/\text{min}$ | 1200 $^\circ\text{C}$ | 3 hr | PbO rich |

Table 2.1: Parameters for synthesis of $\text{PbFe}_{12}\text{O}_{19}$

2.1.2 Synthesis of $\text{Ba}_2\text{Zn}_2\text{Fe}_{12}\text{O}_{22}$

$\text{Ba}_2\text{Zn}_2\text{Fe}_{12}\text{O}_{22}$ was successfully synthesised using solid state synthesis. The raw materials used, BaO (Aldrich, 99.99%), ZnO (Alfa Aesar, 99.9%) and Fe_2O_3 (Sigma Aldrich, 99%) were taken in the molar ratio 1:1:3 respectively, amounting to a total weight of around 1.2 grams. They were mixed using agate mortar and pestle for 2.5 hours. Pellets were made out of the sample, which were sintered in P310 Nabertherm furnace using alumina crucibles. As none of the raw materials are volatile, no special atmosphere was required and the reaction was carried out in normal air atmosphere. The parameters used for the sintering are as given in the table 2.2 The balanced reaction equation is

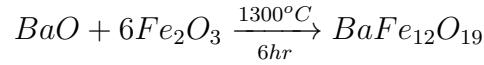


| Heating Rate | Temperature | Time | Environment |
|--------------|-------------|------|-------------|
| 10 °C/min | 1150 °C | 4 hr | Air |

Table 2.2: Parameters for synthesis of $Ba_2Zn_2Fe_{12}O_{22}$

2.1.3 Synthesis of $BaFe_{12}O_{19}$

Solid state synthesis was used for the preparation of $BaFe_{12}O_{19}$. The raw materials used were BaO (Aldrich, 99.99%) and Fe_2O_3 (Sigma Aldrich, 99%), taken in the molar ratio 1:6 respectively. They were mixed well in agate mortar and pestle for 2.5 hours. Pellets were made out of the sample, which were sintered in P310 Nabertherm furnace using alumina crucibles. The parameters used for its synthesis is as given in table 2.3



| Heating Rate | Temperature | Time | Environment |
|--------------|-------------|------|-------------|
| 5 °C/min | 1300 °C | 6 hr | Air |

Table 2.3: Parameters for synthesis of $BaFe_{12}O_{19}$

2.2 X Ray Diffraction (XRD)

XRD is a powerful tool used in the process of characterization and qualitative analysis of the sample prepared. It identifies the phases present in a given sample along with its crystal structure and space group. It works on the principle of elastic scattering of X rays from the electrons in the atoms. When the incident X ray strikes an atom, it acts as a scatterer, acting as a source of secondary X rays. As there are atoms in multiple interplanar layers, they all act as sources of secondary X rays. Many of these X rays cancel each other out due to destructive interference except at few angles which are seen as the peaks in XRD data [3]. The condition for constructive interference is given by the Bragg's law

$$2d\sin(\theta) = n\lambda \tag{2.1}$$

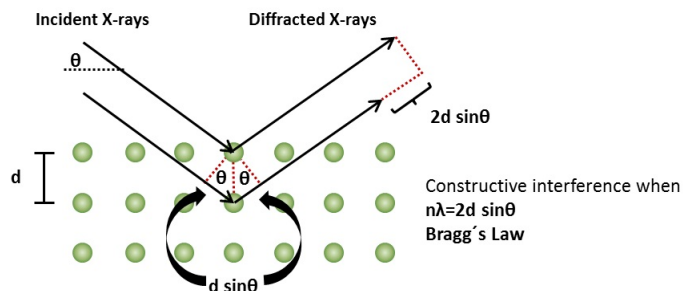


Figure 2.2: Schematic diagram representing Bragg's Law. [63]

where d is the interplanar distance, θ is the scattering, n is the order of reflection and λ is the wavelength of the X ray used.

Bruker D8 Advance Powder X-ray Diffractometer facility at IISER Pune was used to obtain the XRD data of the samples produced. It produces $\text{Cu } k\alpha$ X-rays with wavelength of 0.15406 nm.

It works on $\theta - \theta$ Bragg-Brentano geometry where both the source arm and the detector arm moves theta angle such that the angle between the incident and scattered ray is 2θ . Here the sample is loaded on a glass slide which is mounted on an aluminium sample holder which remains stationary. Before loading of the sample, the sample is well ground to fine powder so as to ensure random orientation of crystalline planes. The sample holder along with sample was also set into rotation to further ensure the exposure of all crystal planes to the X rays. The XRD data obtained were compared with already existing references in Crystallography Open Database (COD)

2.3 Structural Analysis

The structural analysis was carried out using Rietveld refinement. The method is based on least square fitting where refinement is carried out in an iterative manner where various parameters like background, lattice parameters, atomic positions, thermal parameters, instrumental parameters and other shape parameters are varied so as to obtain the optimal values which matches with that that of the obtained data. The Rietveld refinement is carried out in the open software called FullProf [66][55].

During the refinement, the program tries to minimize the function

$$S_y = \sum_i w_i (y_i - y_{ci}) \quad (2.2)$$

y_i = Measured intensity at the i^{th} step

y_{ci} = Calculated intensity at the i^{th} step

$w_i = 1/y_i$

The value of y_{ci} is calculated by the function given by

$$y_{ci} = S \sum_K L_K |F_K|^2 \phi(2\theta_i - \theta_K) P_K A + y_{bi} \quad (2.3)$$

Now let us examine each term one by one

(i) s is the scale factor

(ii) K represents the Miller indices h,k,l for a Bragg reflection

(iii) L_k contains the Lorentz, polarization and multiplicity factors

(iv) $\phi(2\theta_i - 2\theta_K)$ is the reflection profile function. Usually we use the Pseudo-Voigt function as the reflection profile function. Pseudo-Voigt is the linear combination of Gaussian and Lorentzian functions and is given by the equation

$$\theta = \eta L + (1 - \eta) G \quad (2.4)$$

where L is the Lorentzian function, G is the Gaussian function and η is a refinable parameter.

(v) P_K is the preferred orientation function, which is given by the equation

$$P_K = (G_1^2 \cos^2 \alpha + (1/G_1) \sin^2 \alpha)^{-3/2} \quad (2.5)$$

where α and G_1 are refinable parameters. (vi) A is the absorption factor

(vii) F_K is the structure factor for the K^{th} Bragg reflection given by the function

$$F_{hkl} = \sum_i N_i f_i e^{2\pi i(hx_i + ky_i + lz_i)} e^{-8\pi^2 u_i^2 \sin^2 \theta / \lambda^2} \quad (2.6)$$

where

h,k,l = Miller indices of a Bragg reflection

x_i, y_i, z_i = atomic positions of the i^{th} atom

N_i = Site occupancy of the i^{th} atom

f_i = Atomic scattering factor of the i^{th} atom

u_s^2 = Root mean square value of the thermal displacement of the i^{th} atom in a direction parallel to the diffraction vector.

(viii) y_{bi} is the background intensity at the i^{th} step.

Since the function to be minimized is non-linear, the solution is to be found by an iterative procedure. Also inputting a reasonable starting model is necessary in order to avoid any divergence or leading to a local minima.

Now, the Full Width at Half Maximum (FWHM) is represented by H and is given by the equation

$$H^2 = u \tan^2 \theta + v \tan \theta + w \quad (2.7)$$

where u, v, w are refinable parameters.

The quality of the fit is determined by the R values. Among several R values present, the most reliable one is the R_{wp} and is given by

$$R_{wp} = \left[\frac{\sum_i w_i |y_i - y_{ci}|^2}{\sum_i w_i y_i^2} \right]^{1/2} \quad (2.8)$$

Another criterion on the basis of which the fit can be judged on is the 'goodness of fit' parameter Z ,

$$Z = \frac{R_{wp}}{R_e} \quad (2.9)$$

where R_e is the Expected weighted profile factor, given by

$$R_e = \left[\frac{n - p}{\sum_i w_i y_i^2} \right]^{1/2} \quad (2.10)$$

where n is the number of points in the pattern and p is the number of refined parameters. So $n-p$ represents the number of degrees of freedom. [66] [55]

2.4 Field Emission Scanning Electron (FE SEM) and Energy Dispersion X ray (EDX)

Field Emission Scanning Electron Microscopy (FE SEM) provides high resolution images of the topography of a material. It consists of an electron source from which electrons are ejected, which are then accelerated to high velocities with the help of an electric field gradient[38]. These electrons are called primary electrons and these primary electrons are then focused on to a small patch of the sample with the help of magnetic lenses. This bombardment of the surface of the sample with primary electrons leads to ejection of electrons from the surface of the specimen and these are called secondary electrons. The velocity and direction of these ejected secondary electrons are a function of the morphology of the surface at that area. These secondary electrons are collected by a detector and processed into a 3 D image of the sample [16]. The beam of primary electrons scan over the surfaces in a raster pattern to obtain the full images. Energy Dispersion X ray spectroscopy is a characterization technique used to find the elemental composition and their relative ratios in the sample. High energy electrons are bombarded onto the sample which causes the electrons in the inner most shell of the atoms to get excited. This leaves a vacancy in the inner most shell, which is quickly taken over by higher shell electrons. This results in the emission of X rays of particular frequencies. This emitted electrons are picked up and converted to electrical voltage spectrum. Now different elements have different spectrum from which we could identify the elements present. ZEISS Ultra Plus Field Emission Scanning Electron Microscope was used to obtain images and carry out EDX measurements on the samples.

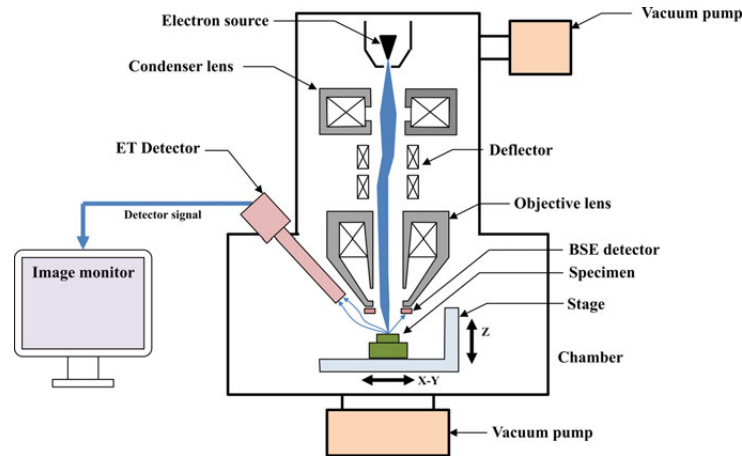


Figure 2.3: Schematic diagram of scanning electron microscope [30].

2.5 Leaching

Leaching is the process of separating components of a mixture based on the idea that some components are soluble in a suitable solvent while others are insoluble. The insoluble component can be separated by filtration or some other method. The soluble component can then be extracted by evaporating or boiling off the solvent [26] [51].

2.6 Magnetron sputtering

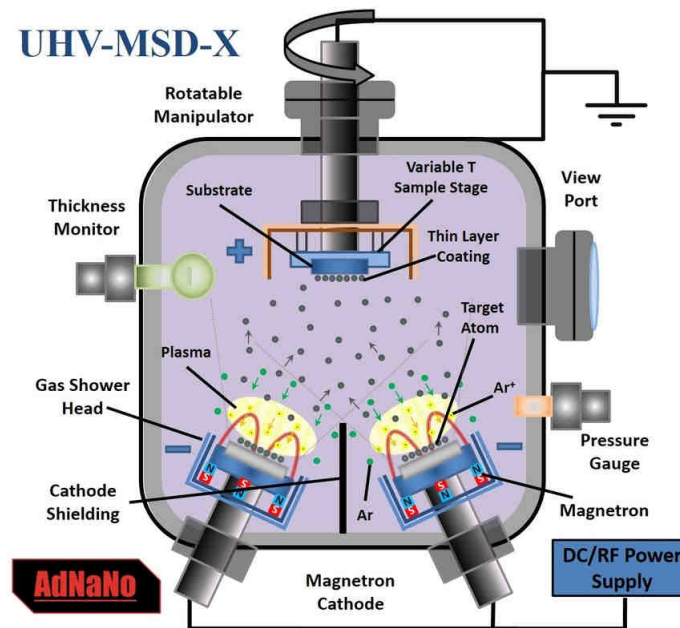


Figure 2.4: Schematic diagram showing the working of a DC Magnetron sputtering system [2].

Magnetron sputtering is a Physical Vapour Deposition (PVD) method used for producing thin films and coatings [29]. The “target” is the source of the material which is deposited on the substrate or sample. The target and the substrate are both kept inside a vacuum chamber and the sputtering gas, usually argon or xenon is pumped in small quantities. The target act as the cathode and a cap placed slightly over the target act as the anode. A potential is applied across the electrodes which ionises the argon gas. The positively charged argon gas now get attracted towards the negatively charged target material thereby sputtering off

some target material off its surface. The potential should be high enough so as to accelerate the argon ions to high velocities such that they chip off materials off the surface of target. The material ejected could fly off in any direction thus making the process ineffective. So as to direct the ejected materials towards the substrate, a magnetic field is used. The magnetic field has other advantages like it helps in ionization of argon gas by a process called as ion trapping.

Here at IISER Pune, Moorfield Minilab Deposition System Type ST80A was used to deposit platinum of thickness 90 nm over the slabs made out of the samples.

2.7 Atomic Force Microscope (AFM)

Atomic Force Microscope [9] is a powerful imaging technique that is a type of Scanning probing microscopy and can be used to visualise the topography of materials on a nanoscale regime. It consists of a nanoscopic tip that is attached to a cantilever. The fine tip scans over the surface of the material, thus bending the cantilever. The amount of bending of the cantilever is sensed using laser and detectors and the signal is processed to obtain the surface morphology of the sample. The height of the cantilever is also adjusted so as to not bend it beyond its breaking point.

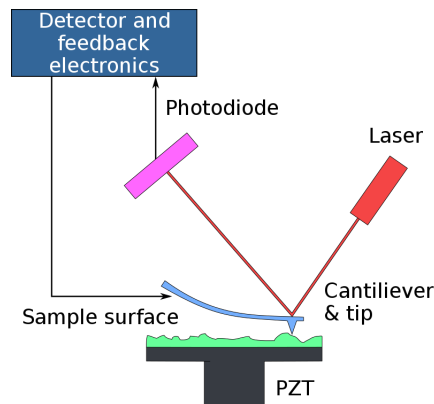


Figure 2.5: Working of atomic force microscope [62].

Before sputtering platinum on top of the sample, a calibration on the sputtering system needs to be done so as to make sure 90 nm thickness platinum is coated. This is done by depositing platinum on top of a sapphire substrate. A scratch is then induced in the coating.

It is then scanned under AFM to measure thickness of the platinum layer coated.

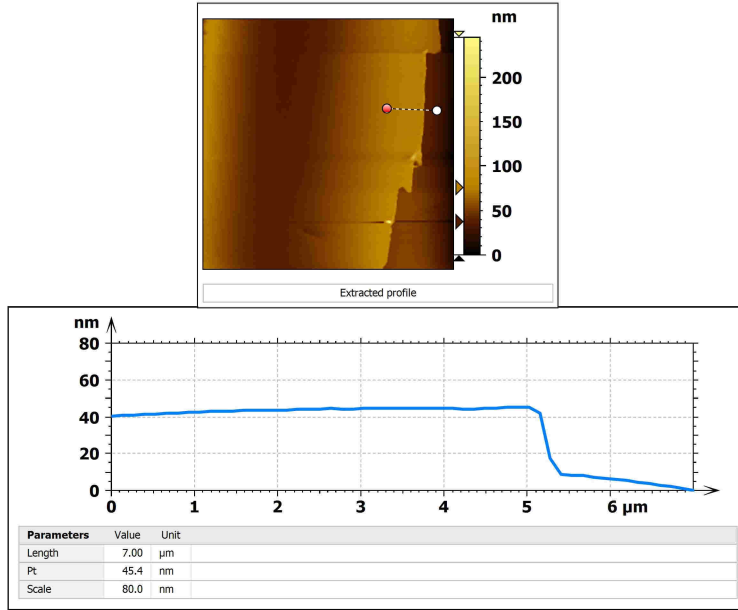


Figure 2.6: Platinum deposited on sapphire substrate under AFM. The thickness was measure to be roughly 40 nm.

2.8 Dielectric measurements

Dielectrics are materials that are poor conductors of electricity hence making them ideal for storing charges by applying electric field through the material. This ability to store charges is quantified by the dielectric constant (K) of the material. It is also called as relative permittivity (ϵ_r) of the material which is defined at the ratio of the absolute permittivity of the material (ϵ) to the absolute permittivity of vacuum (ϵ_0) [28] [47].

$$\epsilon_r = \epsilon / \epsilon_0 \quad (2.11)$$

Experimentally, the dielectric constant or relative permittivity is found using a parallel plate capacitor and it is defined as the ratio of capacitance with the medium in between the parallel plates to the capacitance with vacuum in between the plates.

$$K = \epsilon_r = \frac{C}{C_0} = \frac{\epsilon}{\epsilon_0} \quad (2.12)$$

where C is the capacitance with the medium in between and C_0 is the capacitance with vacuum in between. Capacitance is a complex value which can be written as the sum of a real part and an imaginary part.

$$\epsilon_r = \epsilon_r' + i\epsilon_r'' \quad (2.13)$$

The ratio between the imaginary part real part is called the dielectric loss or the loss tangent.

$$\tan(\delta) = \frac{\epsilon_r''}{\epsilon_r'} \quad (2.14)$$

The dielectric loss accounts for the inherent dissipation of energy in a dielectric material when subjected to a changing external electric field [28]. Both the real part and imaginary part of dielectric constant depends on the temperature as well as the frequency of the AC voltage applied across the parallel plates. Linear dielectrics are materials in which the polarization induced is directly proportional to the electric field applied. But at high field strengths, the linearity no longer holds and higher orders of electric field are involved. Here the focus is on linear dielectric.

The dielectric measurements were carried out on a home built setup which consists of a Alpha-A high frequency analyzer (Novocontrol Technologies) to measure the frequency dependence of the dielectric constants at different temperatures. A CCR (Cryo Industries of America, Model-204-N) was used to bring the sample temperature to as low as 18 K. A programmable heater was used to control the temperature of the cold head and the sample. For performing the measurement, a pellet of the sample was made and silver paste was applied on either side of the pellets which act as the parallel plates of the capacitor. Copper wires were attached on there parallel plates using silver paste. Then the surfaces were furteh covered with silver paste to make the contacts more firm. This pellet is then attached to the copper plate with the help of apiezon grease and cigarette paper, which provides thermal conduction while maintaining electrical insulation.

2.9 Spin Seebeck Measurement

The slabs of the sample were prepared and subjected to measurement of the Longitudinal Spin Seebeck (LSSE) signal using a home made experimental apparatus. The apparatus consists of a closed cycle refrigerator (CCR) - (Advanced Research Systems model number:

DE202), a temperature controller (Lakeshore 336), a nanovoltmeter, a source meter, and an electromagnet with an upper field limit of 2 kOe. The temperature gradient across the sample, as well as the average temperature of the sample, are regulated by two PID controlled heaters and monitored by two cernox sensors placed near the sample's edge. The holder's geometry ensures that the applied thermal gradient is always orthogonal to the magnetic field's rotation plane. The entire setup is enclosed within a Faraday cage to minimize noise, thus bring down the noise floor to 10 nV.

For the SSE measurements, the sample is made into pellet and a slab was cut out of it. Using the Sputtering unit, a layer of platinum of thickness 70 nm was deposited on top of the slab as given in the figure 2.7a. The top surface of the sample was completely coated with platinum. Using silver paste and gold wire of diameter 125 micron, contacts were made on either sides of the slab as given in the figure 2.7a

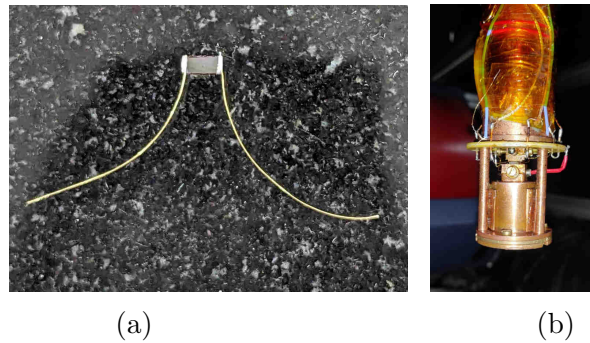


Figure 2.7: (a) Platinum deposited on BaY with gold wire attached to the sample using silver paste. (b) Image of the sample holder

This slab is loaded into the sample holder of the SSE setup. The loading of the sample onto sample holder is a delicate process and care has to be taken so as to load properly. The sample needs to be properly anchored to the sample holder and for doing that, we sandwich it between two copper blocks. So as to avoid giving pressure to the contact and to provide proper anchoring, a piece of sapphire is placed on top of the sample between the contacts such that it does not touch the contacts and at the same time lies close to the contacts. It is held in place with the help of apiezon grease. The sapphire as well as the apiezon grease are good thermal conductors which facilitate the establishment of a thermal gradient across the sample. The sample has to be electrically isolated so as to eliminate all unwanted signals. For increasing the electrical isolation, a cigarette paper soaked in ge varnish is placed over the surface of the copper blocks of the sample holder. A screw is used to tight the copper

blocks and the sample in position so as to reduce noise induced by the CCR cycles. Once the sample is loaded, a temperature gradient is applied across the sample with the help of 2 heaters in the copper block on either side of the sample and controlled by a temperature controller.

2.10 Resistivity measurements

The resistance of a material is generally given by the formula

$$R = \frac{V}{I} \quad (2.15)$$

where V is the voltage applied across a sample or material and I is the current passing through it. Resistance is an extensive property but resistivity or conductance is an intensive property and the resistivity of the material is given by the equation

$$\rho = R \frac{A}{l} \quad (2.16)$$

where R is the resistance of the sample, A is the area of cross section of the material and l is the length of the material.

Resistivity is a temperature dependent property and in insulators and semiconductors, it decreases with rise in temperature. This is because in insulators and semiconductors, conduction happens due to electrons hopping from valence band into conduction band when they get an energy boost [20]. So when temperature increases, more electrons in the valence band will acquire the necessary energy to cross the band gap to reach the conduction band. There are various modes of conduction depending on the material and temperature. In hexaferrites, it is reported to be by electron hopping [36]. Hexaferrites consist of Fe^{3+} ions but occasionally due to lack of oxidising environment during the reaction, Fe^{2+} can form. This results in hopping of an electron from Fe^{2+} to adjacent Fe^{3+} and this process can carry on resulting in a flow of charge.

Various models of electron transport have been developed to explain the behaviour of conductivity of materials under different temperature. In hexaferrites at high temperatures

(250 K to 400 K), Correlated Barrier Hopping (CBH) is considered to be the most suitable to explain the behaviour conductivity [36]. In CBH model, the conduction happens via single polarons or bipolaron hopping process over a Coulomb barrier that separates two defect centers [8]. In these situations, Arrhenius equation can be used to explain the relationship between resistivity and temperature.

$$\rho = \rho_0 \exp\left\{\frac{E_a}{K_b T}\right\} \quad (2.17)$$

where ρ_0 is a pre-exponential factor, E_a is the activation energy, K_b is the Boltzmann constant, and T is the temperature of the material.

If we take log on both sides of the equation, we get

$$\ln(\rho) = \ln(\rho_0) + \frac{E_a}{K_b T} \quad (2.18)$$

So a graph between $\ln(\rho)$ vs $1/T$ will be a straight line having a positive slope. Doing a fitting on the data will give us the pre-exponential factor as well as the activation energy at that temperature.

At low temperatures (150 K to 250 K), Non-overlapping Small Polaron Tunnelling (NSPT) is best known to explain the conductivity behaviour. The relationship between resistivity and temperature is given by the Mott equation [36].

$$\rho = \rho_0 \exp\left\{\left(\frac{T_0}{T}\right)^{1/4}\right\} \quad (2.19)$$

where ρ_0 is a pre-exponential factor, T_0 is a parameter called characteristic temperature, and T is the temperature of the material.

If we take log on both sides of the equation, we get

$$\ln(\rho) = \ln(\rho_0) + \left(\frac{T_0}{T}\right)^{1/4} \quad (2.20)$$

So a graph between $\ln(\rho)$ vs $1/T^{1/4}$ will be a straight line having a positive slope. Doing a fitting on the data will give us the pre-exponential factor as well as the characteristic temperature T_0 . The parameter T_0 is not a constant but instead varies with temperature.

The resistivity of the samples were measured on the Spin Seebeck measurement unit using a two probe setup[60]. For the resistivity measurements, the sample is made into a

pellet and a slab was cut out from it. On either sides of the slab, silver paint was applied and then gold wire was used to make contact on either sides of the slab. It is then loaded onto the sample holder and kept in place by the copper blocks. The electrical isolation of the sample from the copper blocks was achieved by sapphire pieces and apiezon grease, which are thermally conducting and electrically insulating.

Chapter 3

Results and Discussion

3.1 Synthesis and XRD analysis

3.1.1 $\text{PbFe}_{12}\text{O}_{19}$

The synthesis of $\text{PbFe}_{12}\text{O}_{19}$ was carried out using solid state synthesis (section 2.1.1). The XRD data of the sample was obtained and compared with the reference data of $\text{SrFe}_{12}\text{O}_{19}$ obtained from Crystallography Open Database (COD) (COD ID: 1006000) since the reference data of $\text{PbFe}_{12}\text{O}_{19}$ was not available. It is reported that the crystal structure remains more or less the same when Sr is replaced by Ba or Pb, and the lattice parameters changes by only a small factor [43]. So it is safe to assume that the XRD reference of $\text{SrFe}_{12}\text{O}_{19}$ could be used for identifying $\text{PbFe}_{12}\text{O}_{19}$.

Comparison showed that although the peak positions were matching, peak intensities and peak shape differed considerably. In some positions, the peaks were broadened (see image 3.1). First assumption was that it might be due to the different divalent cations used in the sample and in reference. For a confirmation, EDX measurement was performed on the sample on multiple areas and their average was taken. The theoretical atomic ratio of Pb:Fe is 7.69 : 92.31 but the data obtained was 18.15 ± 0.38 : 81.85. Thus it was concluded that excess of Pb was present. The FE SEM images also supported impure phases in the sample as shown in figures 3.2 .

One interesting property of PbO is that when part of a homogeneous mixture with other

compounds, when XRD is performed on it, the PbO peaks are suppressed. This was observed when XRD of reactant after grinding for 3 hours was taken. The result was an XRD data in which Fe_2O_3 peaks were prominent and PbO peaks in minor. The reason could be due to high absorbance of X ray wavelengths by the Pb atom as reported in literature [17] [45]. The observation of excess PbO could be attributed to the deposition of PbO on the pellet when kept in the PbO rich atmosphere. This assumption was supported by the quantitative measurements, ie the weight of the pellet after sintering was always found to be more than that before sintering.

To get rid of the excess PbO, leaching was performed. Leaching is the process of separating components of a mixture based on the idea that some components are soluble in a suitable solvent while others are insoluble. Earlier papers reported leaching using HCl as an effective method for purifying BaM from BaFe_2O_4 [51]. BaFe_2O_4 dissolves in HCl while BaM remains intact. Apart from dissolving BaFe_2O_4 , HCl is also well known for dissolving metal oxides in metallurgy. As a result, HCl was chosen as the solvent for leaching. 20ml of HCl was dissolved in 200ml of millipore water and around 1g of sintered sample was ground and added to the solution. It was stirred using magnetic bead for around 8hr. It was observed that the solution turned yellow in color while the undissolved sample clung around the magnetic bead. The yellow solution was drained off, retaining the sample, which was later dried under IR lamp. XRD was performed on this sample which revealed that leaching has indeed worked as the reference data intensities more or less matched and the peaks appeared sharper (see figure 3.1). EDX measurement was also taken which further confirmed the purity of the sample. The measured ratio of Pb:Fe was obtained to be $(7.08 \pm 0.15) : 92.92$ and the image 3.3 also appear to be clean.

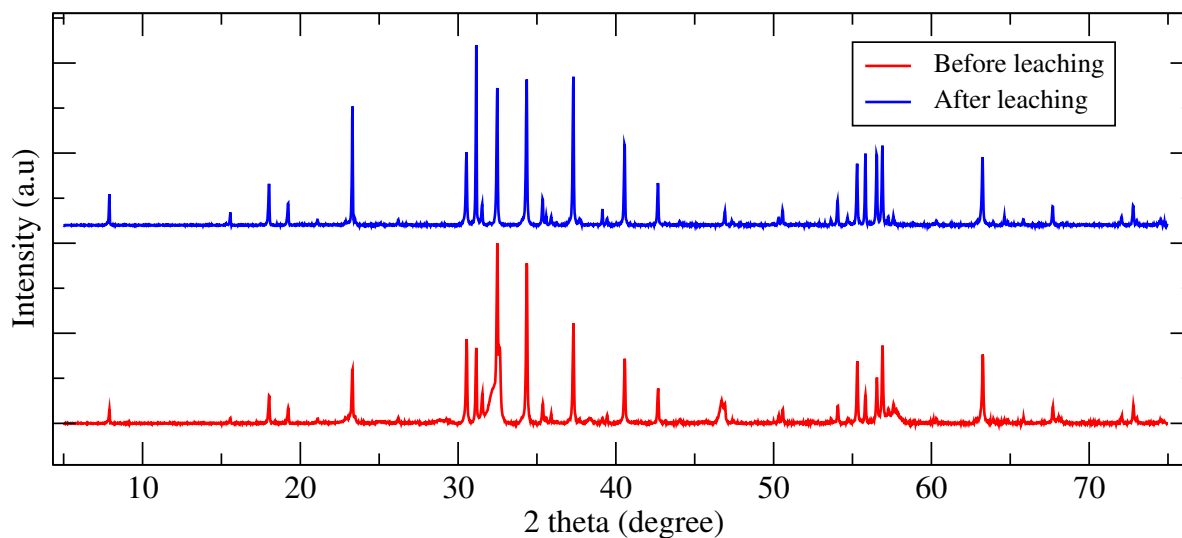


Figure 3.1: XRD data of $\text{PbFe}_{12}\text{O}_{19}$ before and after leaching

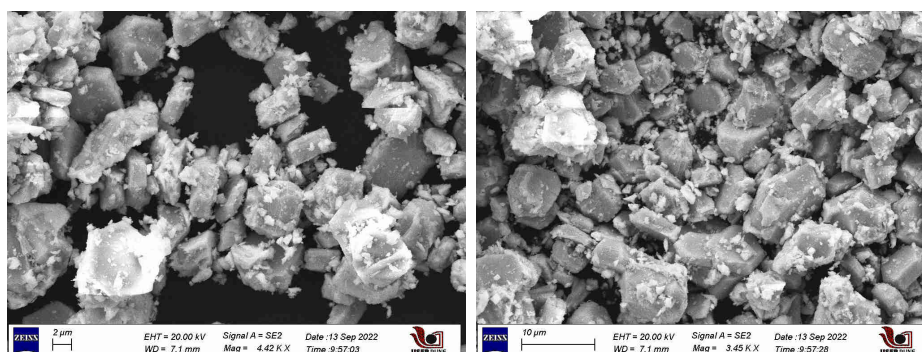


Figure 3.2: FE SEM images after leaching. We can see grains of the sample along with a lot of impurities

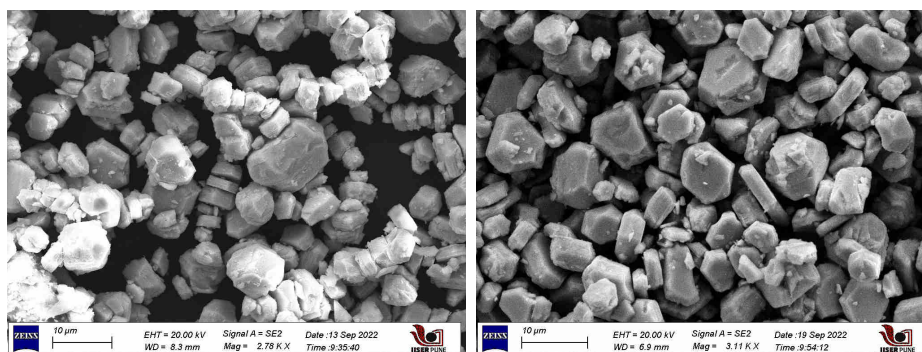


Figure 3.3: FE SEM images after leaching. Compared to the images before leaching, no impurities seem to present along with the grains.

| | |
|-----------------|----------------------|
| Before leaching | 18.15 ± 0.38 : 81.85 |
| After leaching | 7.08 ± 0.15 : 92.92 |
| Ideal ratio | 7.69 : 92.31 |

Table 3.1: Table demonstrating the change in atomic ratio of Pb : Fe before and after leaching

From the pure sample, a pellet was made and a 2nd sintering at a temperature of 1100°C for densification was performed. But it was found that the sample decomposed and the PbO vapourised leaving behind Fe₂O₃. So a lower temperature was chosen for densification but the resulting pellet was too soft to be made into a slab for measurement. To overcome this issue, the slab was chosen to be made out of the pellet after 1st heat treatment and to remove the excess PbO from the sample, the pellet was polished to remove the few layers which contain excess PbO. A trial sample was made and was observed to contain Pb : Fe ratio close to that of the ideal value. So more slabs were prepared following this protocol. For the final sample, the atomic ratio of Pb : Fe was found to be 7.50±0.8 : 92.50.

3.1.2 Ba₂Zn₂Fe₁₂O₂₂

Synthesis of Ba₂Zn₂Fe₁₂O₂₂ was carried using solid state synthesis (section 2.1.2). The XRD was performed and data was obtained as given in figure 3.4. No extra phases were observed. The global EDX taken from large areas of sample showed an average atomic ratio of Ba : Zn : Fe as (13.59 ± 0.07) : (12.36 ± 0.14) : (74.05 ± 0.14), while the ideal ratio being 12.5 : 12.5 : 75. The local EDX taken from individual grains showed a similar ratio. Pellets were made out of the pure sample and a second heat treatment was done on them at 1100°C for 3 hours to obtain a hard pellet from which slabs were cut out.

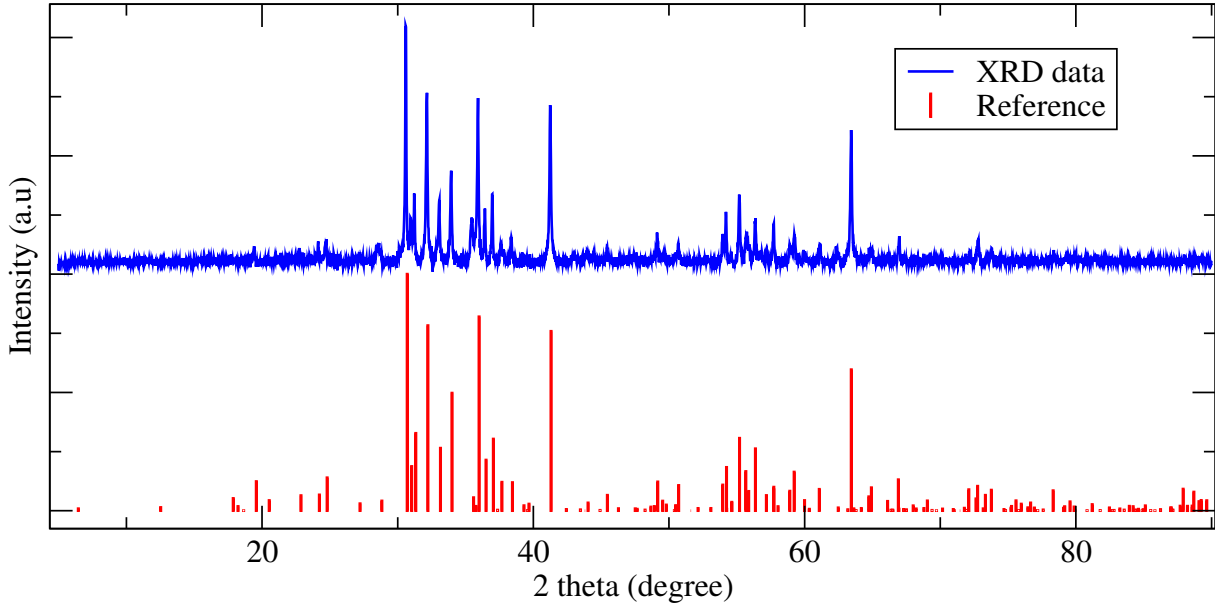


Figure 3.4: XRD data of $\text{Ba}_2\text{Zn}_2\text{Fe}_{12}\text{O}_{22}$ compared to the reference data. No extra peaks were observed.

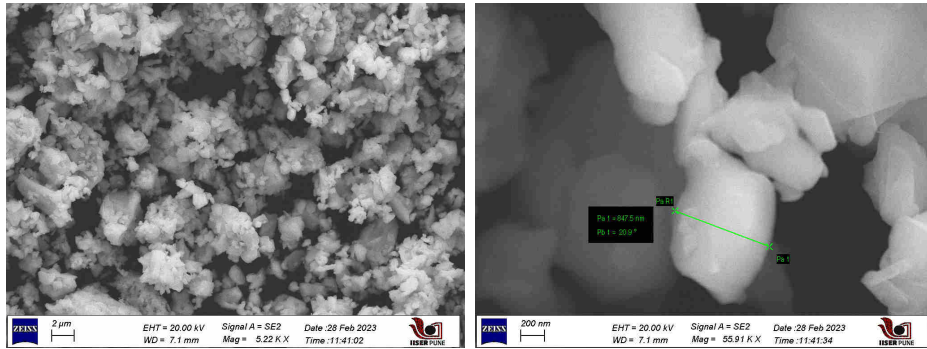


Figure 3.5: FE SEM images of BaY and the size of individual grains

3.1.3 $\text{BaFe}_{12}\text{O}_{19}$

$\text{BaFe}_{12}\text{O}_{19}$ was prepared using solid state synthesis (section 2.1.3). The XRD data confirmed the formation of a pure sample. The global EDX shows an atomic ratio of Ba : Fe as $(8.07 \pm 0.05) : 91.93$, the ideal being $7.69 : 92.31$. The local EDX taken over individual grains also showed a similar ratio. As we aim to compare the SSE on BaM and PbM, care has to be taken keep other properties of the samples same. So slabs were prepared using the same protocols used for making PbM slabs.

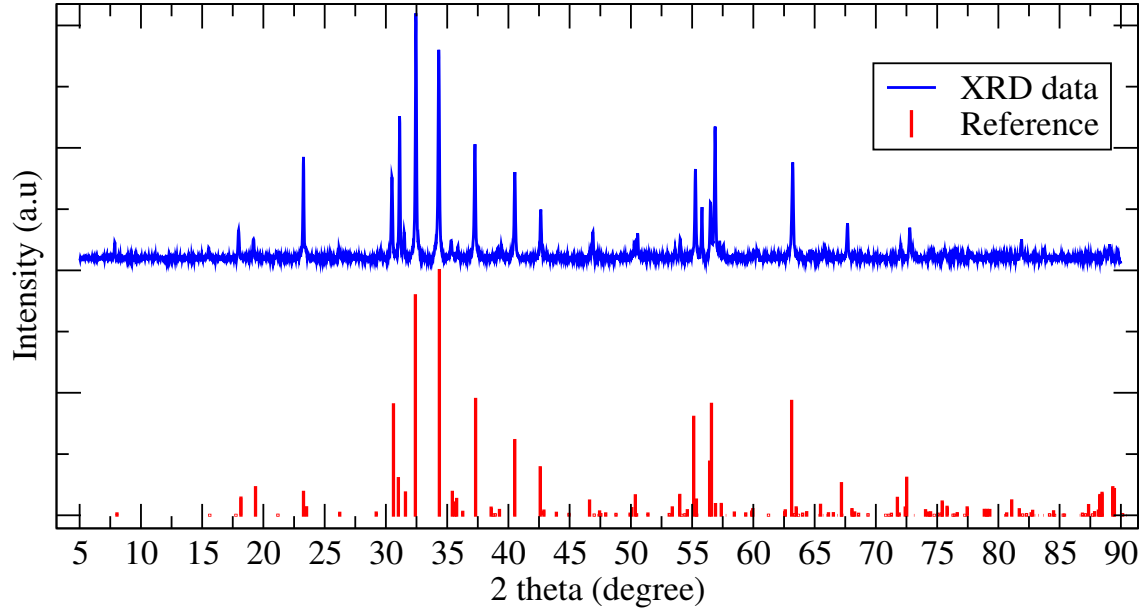


Figure 3.6: XRD data of $\text{BaFe}_{12}\text{O}_{19}$ compared to the reference data. No extra peaks were observed. The intensity of some peaks do not match which can be attributed to the preferred orientation of the grains

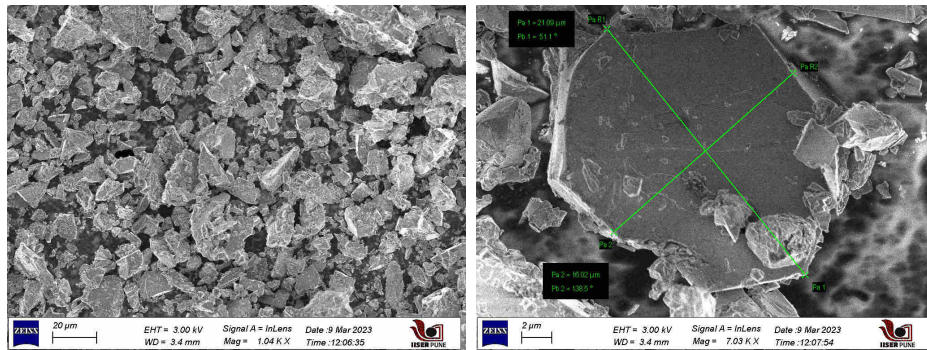


Figure 3.7: FE SEM images of BaM and the size of individual grains

3.2 Structural Refinement

3.2.1 $\text{PbFe}_{12}\text{O}_{19}$

Structural analysis using Rietveld analysis was carried out in FullProf software. As the reference file for $\text{PbFe}_{12}\text{O}_{19}$ as not available, the reference file used was that of $\text{BaFe}_{12}\text{O}_{19}$.

As there is some structural difference between PbM and BaM, the least fit (given in figure 3.8) was hard to obtain and the best value of χ^2 obtained was 6.34. The refined lattice parameters are as given in table 3.2 and that of the atomic positions are given in table 3.3. The reported values of lattice parameters of $\text{PbFe}_{12}\text{O}_{19}$ are $a=b = 5.894 \text{ \AA}$, $c = 23.106 \text{ \AA}$ [40]. As we can see from the table 3.2, the refined lattice parameters for a and b are matching up to 2 decimal places but for that of c, it matches up to one decimal place. Several literatures have provided varying values for the lattice parameters, which coincide with each other up to only one decimal place. Therefore, it is unfeasible to establish a precise standard value for the lattice parameters.

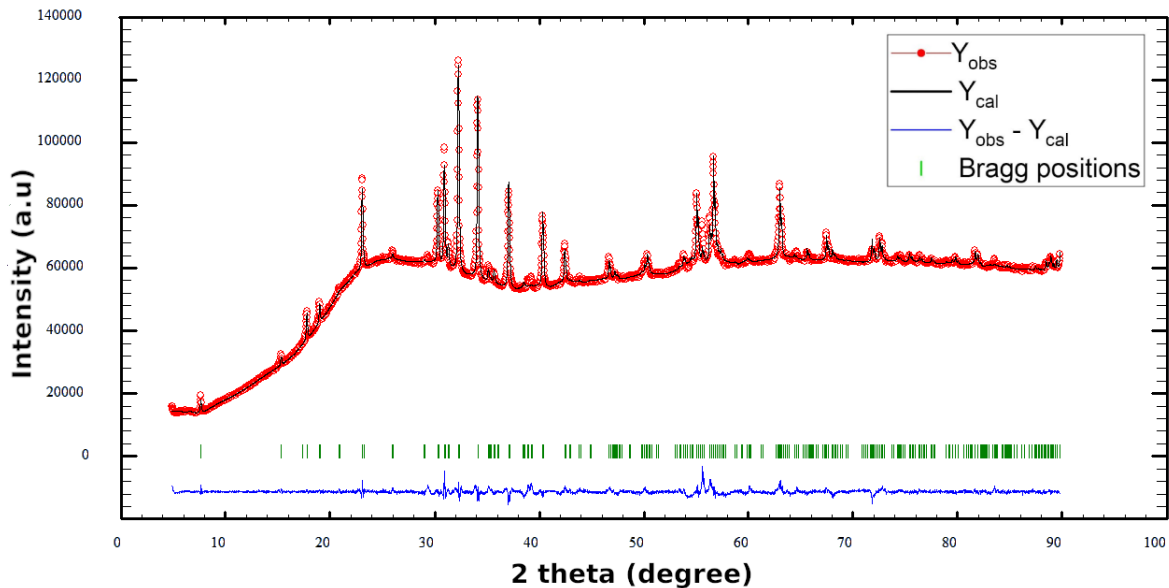


Figure 3.8: Rietveld refinement plot for PbM

| | | | | |
|------------------------------------|------------------------|--------------------------------|---|--------------------------------|
| Chemical Formula: | | Molecular Weight: | Temperature: | |
| PbFe ₁₂ O ₁₉ | | 1181.321 g/mol | 24 °C | |
| Crystal Structure: | | Space Group and Number: | | |
| Hexagonal | | P63/mmc, 194 | | |
| Unit Cell Parameters | | | | |
| a (Å): | b (Å): | c (Å): | α, β, γ, (degree): | Volume (Å³): |
| 5.896(7) | 5.896(7) | 23.126(6) | 90,90,120 | 2089.233(8) |
| χ^2: | R_{wp}: | R_e: | Goodness of fit (R_{wp}/R_e) | |
| 6.34 | 15.3 | 6.08 | 2.52 | |

Table 3.2: Refined lattice and fitting parameters for PbFe₁₂O₁₉

| Atom | x/a | y/b | z/c | Fractional Occupancy |
|------|---------|---------|----------|----------------------|
| Pb1 | 0.6667 | 0.3333 | 0.25 | 0.10057 |
| Fe1 | 0 | 0 | 0 | 0.08765 |
| Fe2 | 0 | 0 | 0.26096 | 0.08965 |
| Fe3 | 0.3333 | 0.6667 | 0.02737 | 0.16281 |
| Fe4 | 0.3333 | 0.6667 | 0.19471 | 0.15834 |
| Fe5 | 0.17216 | 0.34435 | -0.10915 | 0.57241 |
| O1 | 0 | 0 | 0.14141 | 0.27789 |
| O2 | 0.3333 | 0.6667 | -0.06889 | 0.25972 |
| O3 | 0.17973 | 0.35946 | 0.25 | 0.42302 |
| O4 | 0.15794 | 0.31587 | 0.04605 | 0.51562 |
| O5 | 0.48335 | 0.96668 | 0.12998 | 0.71046 |

Table 3.3: Refined atomic positions and site occupancy

3.2.2 Ba₂Zn₂Fe₁₂O₂₂

Rietveld analysis on the XRD data was performed using FullProf software. Excellent fits were obtained with χ^2 value of 2.02 as given in figure 3.9 The refined lattice parameters are as given in table 3.4 and that of the atomic positions are given in table 3.5. The reported values of lattice parameters of Ba₂Zn₂Fe₁₂O₂₂ are a = b = 5.8763 Å and c = 43.566 Å [49], and comparing to the refined parameters in table 3.4, they match up to 2 decimal places for the parameters a and b and up to one decimal place for the parameter c.

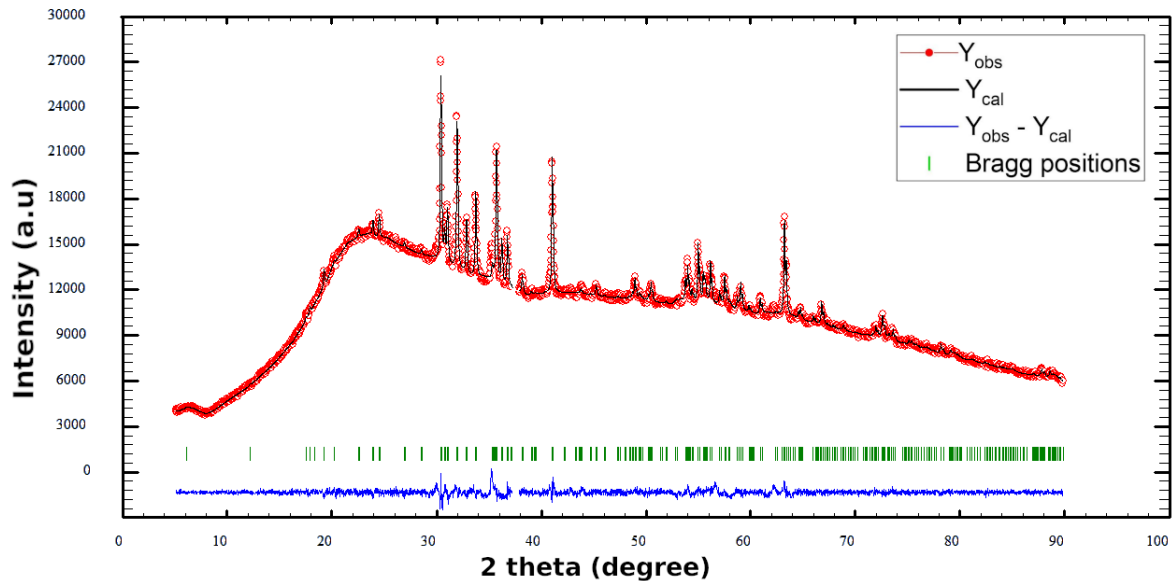


Figure 3.9: Rietveld refinement plot for BaY

| | | |
|--|--------------------------|---------------------|
| Chemical Formula: | Molecular Weight: | Temperature: |
| Ba ₂ Zn ₂ Fe ₁₂ O ₂₂ | 1427.532 g/mol | 24 °C |

| | |
|---------------------------|--------------------------------|
| Crystal Structure: | Space Group and Number: |
| Rhombohedral | R $\bar{3}m$, 166 |

| Unit Cell Parameters | | | | |
|----------------------|---------------|---------------|--|--------------------------------|
| a (Å): | b (Å): | c (Å): | α, β, γ, (degree): | Volume (Å³): |
| 5.878(1) | 5.878(1) | 43.576(1) | 90,90,120 | 3911.725(7) |

| | | | |
|-----------------------------|------------------------|-----------------------|--|
| χ^2: | R_{wp}: | R_e: | Goodness of fit (R_{wp}/R_e): |
| 2.02 | 19.7 | 13.83 | 1.42 |

Table 3.4: Refined lattice and fitting parameters for Ba₂Zn₂Fe₁₂O₂₂

| Atom | x/a | y/b | z/c | Fractional Occupancy |
|------|---------|----------|---------|----------------------|
| Ba1 | 0 | 0 | 0.30009 | 0.16226 |
| Fe1 | 0 | 0 | 0.37659 | 0.16588 |
| Zn1 | 0 | 0 | 0.15234 | 0.04478 |
| Fe2 | 0 | 0 | 0.15234 | 0.13333 |
| Fe3 | 0 | 0 | 0.06732 | 0.175 |
| Zn2 | 0 | 0 | 0.5 | 0.00353 |
| Fe4 | 0 | 0 | 0.5 | 0.07569 |
| Zn3 | 0.50189 | -0.50189 | 0.10969 | 0.11628 |
| Fe5 | 0.50189 | -0.50189 | 0.10969 | 0.40016 |
| Zn4 | 0 | 0 | 0 | 0.02187 |
| Fe6 | 0 | 0 | 0 | 0.0684 |
| O1 | 0 | 0 | 0.41742 | 0.15231 |
| O2 | 0 | 0 | 0.19714 | 0.21542 |
| O3 | 0.15484 | -0.15484 | 0.02985 | 0.5 |
| O4 | 0.82392 | -0.82392 | 0.08399 | 0.5 |
| O5 | 0.16956 | -0.16956 | 0.13688 | 0.5 |

Table 3.5: Refined atomic positions and site occupancy

3.2.3 BaFe₁₂O₁₉

The XRD data was subjected to Rietveld analysis using the FullProf software. Reasonably well fits were obtained with χ^2 value of 3.67 as given in figure 3.10. The refined lattice parameters are as given in table 3.6 and that of the atomic positions are given in table 3.7. The reported values of lattice parameters of BaFe₁₂O₁₉ are $c = 23.183 \text{ \AA}$ and $a = b = 5.8920 \text{ \AA}$ [39]. Comparing with the refined lattice parameters from table 3.6, for the lattice parameter a and b, they match up to 2 decimal places but for the lattice parameter c, they match only in the integer part.

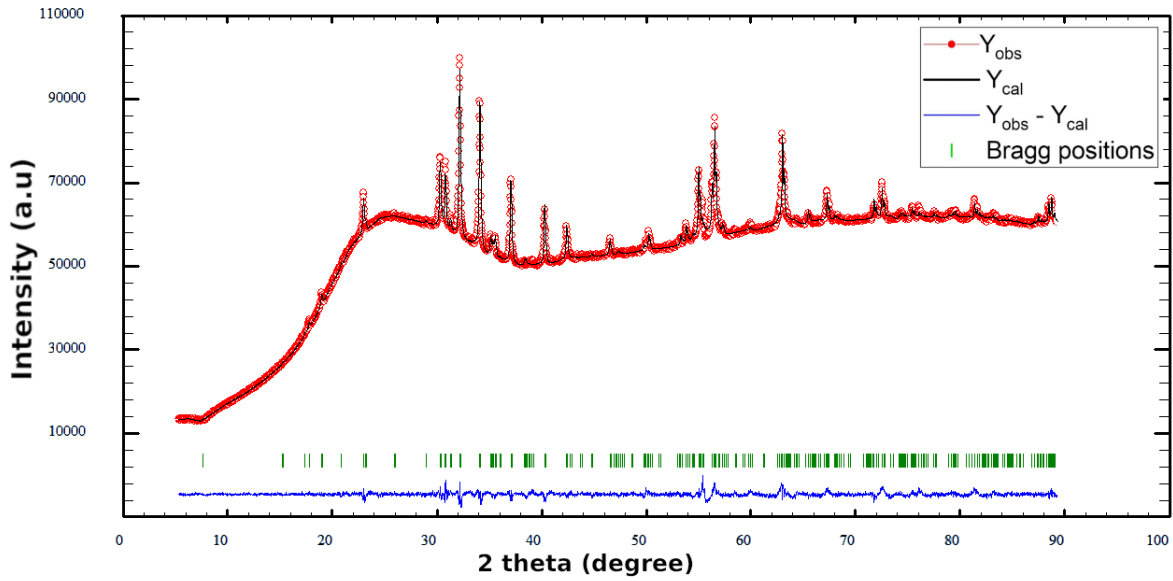


Figure 3.10: Rietveld refinement plot for BaM

| | | |
|------------------------------------|--------------------------|---------------------|
| Chemical Formula: | Molecular Weight: | Temperature: |
| BaFe ₁₂ O ₁₉ | 1111.448 g/mol | 24 °C |

| | |
|---------------------------|--------------------------------|
| Crystal Structure: | Space Group and Number: |
| Hexagonal | P63/mmc, 194 |

| Unit Cell Parameters | | | | |
|----------------------|----------|-----------|-------------------------------------|---------------------------|
| a (Å): | b (Å): | c (Å): | α, β, γ , (degree): | Volume (Å ³): |
| 5.895(1) | 5.895(1) | 23.209(8) | 90,90,120 | 2095.537(7) |

| | | | |
|------------|------------------------|-----------------------|---|
| χ^2 : | R_{wp}: | R_e: | Goodness of fit (R_{wp}/R_e) |
| 3.67 | 16.5 | 8.6 | 1.92 |

Table 3.6: Refined lattice and fitting parameters for BaFe₁₂O₁₉

| Atom | x/a | y/b | z/c | Fractional Occupancy |
|------|---------|---------|----------|----------------------|
| Ba1 | 0.6667 | 0.3333 | 0.25 | 0.07037 |
| Fe1 | 0 | 0 | 0 | 0.06773 |
| Fe2 | 0 | 0 | 0.24937 | 0.07167 |
| Fe3 | 0.3333 | 0.6667 | 0.02602 | 0.16701 |
| Fe4 | 0.3333 | 0.6667 | 0.19609 | 0.16242 |
| Fe5 | 0.16741 | 0.33482 | -0.10879 | 0.51014 |
| O1 | 0 | 0 | 0.13938 | 0.24455 |
| O2 | 0.3333 | 0.6667 | -0.06512 | 0.20886 |
| O3 | 0.23097 | 0.31964 | 0.25 | 0.43775 |
| O4 | 0.19539 | 0.31071 | 0.04573 | 0.61671 |
| O5 | 0.49025 | 0.98047 | 0.14108 | 0.59638 |

Table 3.7: Refined atomic positions and site occupancy

3.3 Resistivity measurements

The resistance of the samples were measured using the two probe technique. The resistance of the sample was found out by applying a voltage across the sample and measuring the corresponding current through the sample. Value of resistance was calculated by taking the ratio of voltage and the corresponding current. For investigating the change in resistivity with temperature, the value of resistance was measured between 13 K to 298 K in step size of 2 K. It was found that the resistance of BaM lies in the range of $10^8\Omega$ and was found to increase with decrease in temperature indicating semiconductor/insulator like behaviour. Once the resistance crossed $10^9\Omega$ below 125 K, it could no longer be measured as it exceeded the range of the apparatus. The length, width and thickness of the slab of BaM was 4.21 mm, 2.21 mm and 0.060 mm respectively. From the raw data of resistance, resistivity was calculated. The obtained resistivity data is as given in figure 3.11

Resistance data was obtained both while cooling the sample from 298 K to 13 K as well as while heating from 13 K to 298 K to check for any hysteresis if present. Upon observation, it was noted that the data from both heating and cooling coincided, leading to the conclusion that there was no hysteresis present.

The experiment was repeated under a magnetic field of 0.2 T to investigate its impact on resistance. The results showed that the curves traced the same path as the previous

experiment without a magnetic field. This led to the conclusion that the magnetic field had no effect on the resistance of the sample.

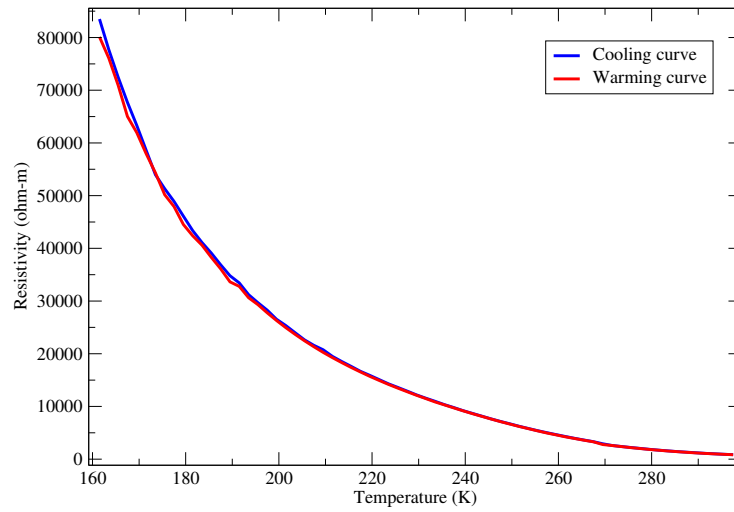


Figure 3.11: Plot of resistivity vs temperature while cooling and warming the BaM sample

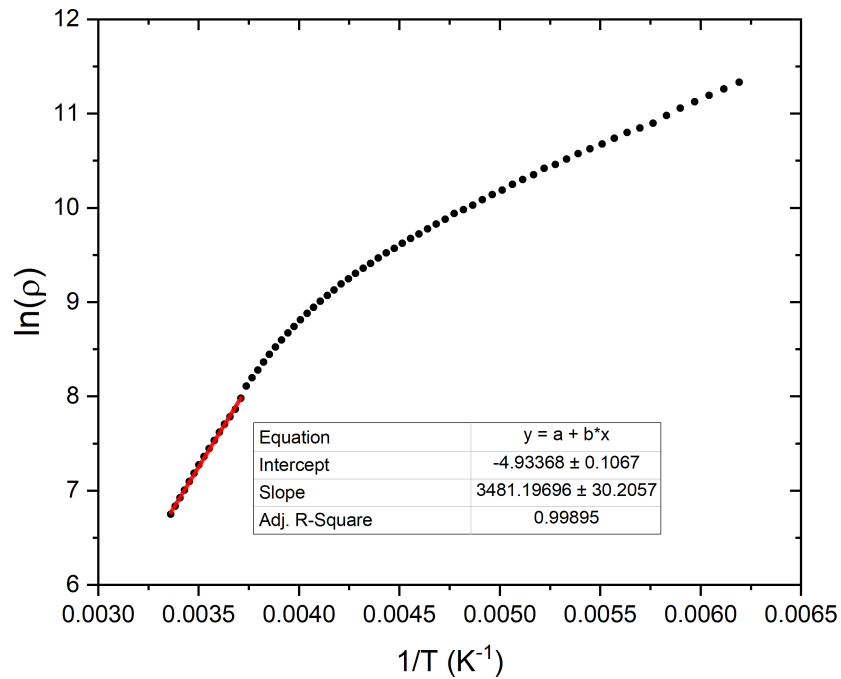


Figure 3.12: Arrhenius fitting was done at high temperature. $\ln(\rho)$ vs $1/T$ was plotted for BaM

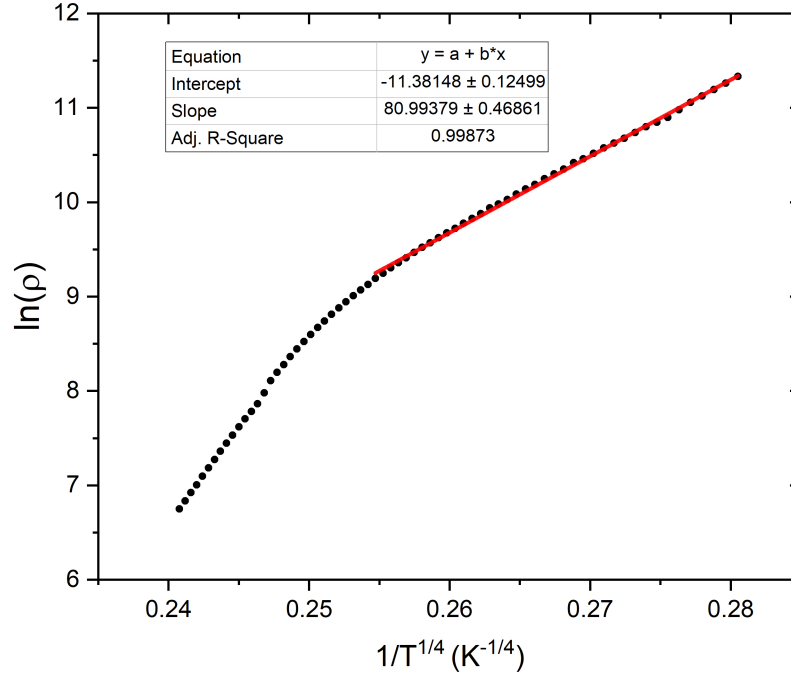


Figure 3.13: Mott fitting was done at low temperature. $\ln(\rho)$ vs $1/T^4$ was plotted for BaM

| | Y intercept | Pre-exponential factor (Ω m) | Slope | T_0 / E_a |
|---------------------------------|-------------|---|--------|---------------------|
| Low temperature (161K-237K) | -11.38 | 1.14×10^{-5} | 80.99 | 4.3×10^7 K |
| High temperature (269K-298K) | -4.93 | 7.23×10^{-3} | 3481.2 | 0.3 eV |

Table 3.8: Fitting parameters and the corresponding physical values

In case of the other samples PbM and BaY, resistance could not be measured as the value of resistance goes beyond the range of the apparatus. The resistivity of poly crystalline bulk samples depends on a lot of factors like density, temperature of sintering etc. So no comparison is possible among the different samples.

3.4 Dielectric measurements

Linear dielectric measurements were carried out on BaM and PbM at temperatures ranging from 18K to 308K with step size of 1K, and frequency sweep ranging from 3Hz to 1MHz at each temperature point. The real part and imaginary part of dielectric constant were measured along with the dielectric loss. The variation of these quantities with temperature for the selected frequencies are as given in the following figures.

3.4.1 BaM

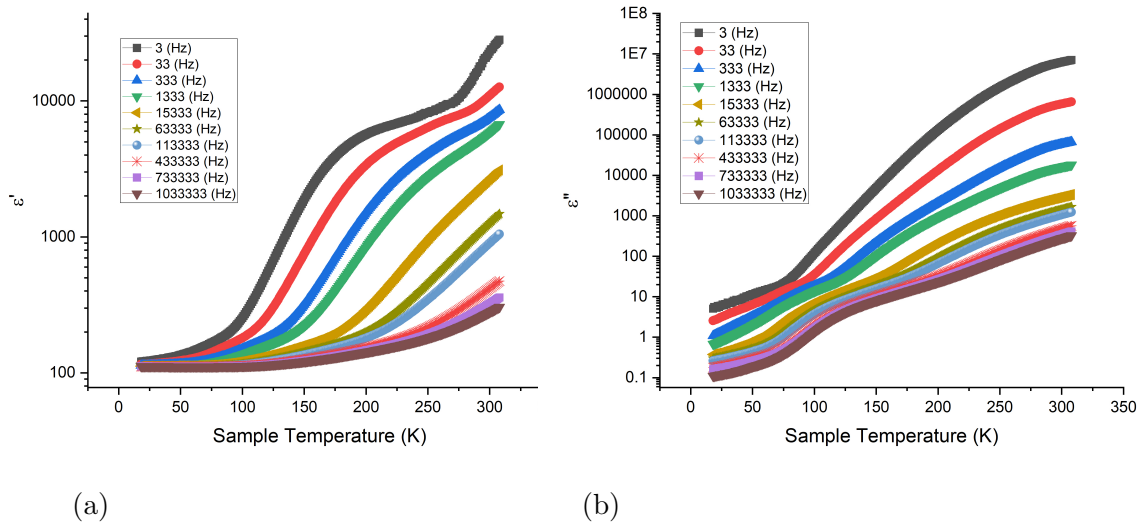


Figure 3.14: (a) Real part of dielectric constant of BaM vs temperature for various frequencies (b) Imaginary part of dielectric constant of BaM vs temperature for various frequencies

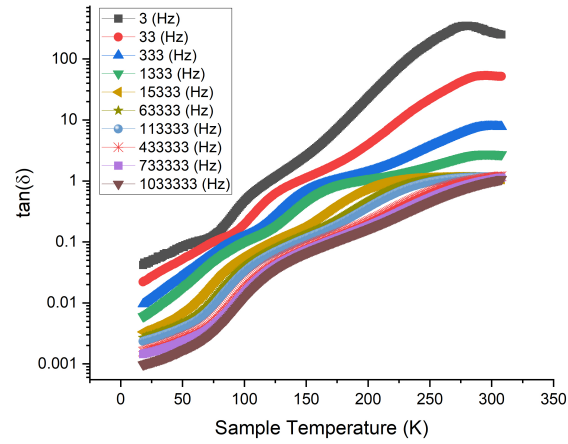


Figure 3.15: Dielectric loss of BaM vs temperature for various frequencies

3.4.2 PbM

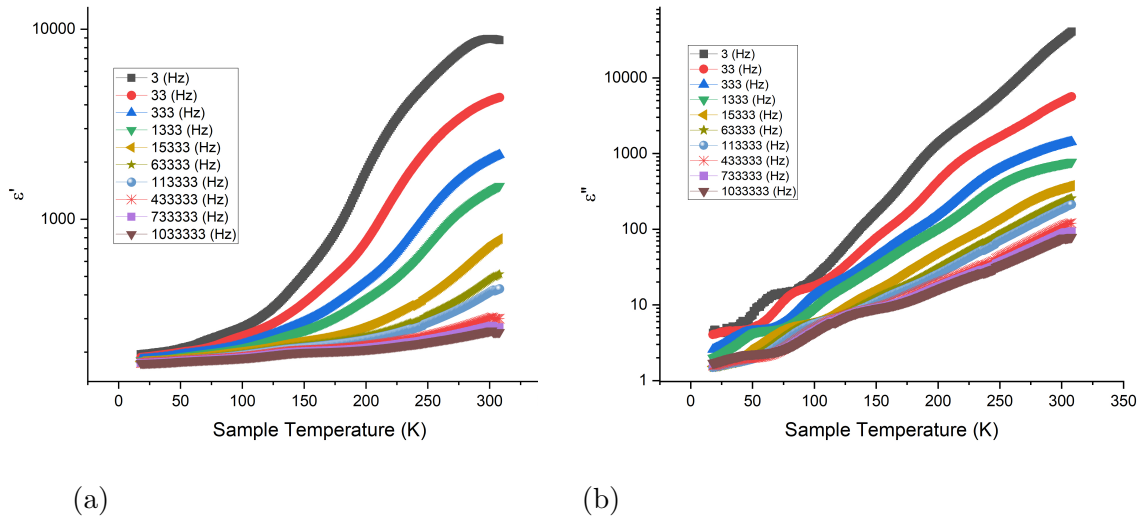


Figure 3.16: (a) Real part of dielectric constant of PbM vs temperature for various frequencies (b) Imaginary part of dielectric constant of PbM vs temperature for various frequencies

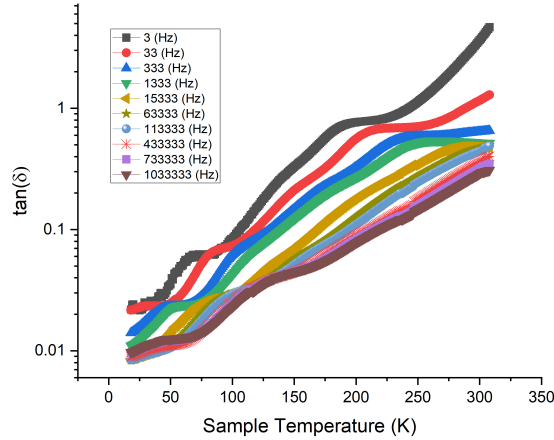


Figure 3.17: Dielectric loss of PbM vs temperature for various frequencies

3.4.3 Temperature dependence of dielectric

As we can see from the graphs above, the real part of dielectric constant increases with temperature in general for all frequencies although not smoothly. This is because as the external electric field is applied, dipoles will be formed in the material and will try to align with the external field. When the temperature is low, the dipoles won't be having enough energy to overcome the barrier to align themselves with the external field. When the temperature is sufficiently high, the dipoles will be able to rotate themselves to align with the external field. But this trend does not go on forever. A point of temperature will be reached called Curie temperature above which the thermal fluctuations become strong enough to disrupt the alignment of these dipoles leading to a decrease in the real part of dielectric constant with temperature [44]. In the case of PbM and BaM, this Curie temperature is well above the room temperature and could not be measured using the instrument. It was also noticed that the dielectric constant of BaM is higher than that of PbM for all the frequencies. The reason for this is currently unknown and more in depth studies are required to gain a more comprehensive understanding.

The dielectric loss originates from 3 different sources, 1) DC current conduction, 2) Space charge migration 3) Movement of molecular dipoles [65]. The imaginary component of dielectric constant increases with temperature for all frequencies because as the temperature increases, the conductivity of the material increases, which in turn causes loss in energy.

It was observed that the dielectric loss of BaM is higher than that of PbM for all the frequencies at a given temperature. This could be explained by the higher resistivity value of PbM compared to BaM, which leads to less conduction of charge carriers.

3.4.4 Frequency dependence of dielectric

Also as we go lower in temperatures, the real part of dielectric constant for both BaM and PbM saturate towards a particular value for all the frequencies suggesting that the frequency doesn't have a significant impact on it at low temperatures. The significance of frequency becomes more prominent at high temperatures. At high temperatures, the real part of dielectric constant decreased rapidly with increase in frequency. This is caused by the reduction of space charge polarization effect at the grain boundaries which is the main contributor to the dielectric constant at low frequencies [44].

The imaginary part of dielectric constant was also found to decrease with increase in frequency. It is attributed to the relaxation time, which is the characteristic time it takes for the material's dipoles or charges to align with the field. At low frequencies, the relaxation time is shorter compared to the period of the applied electric field, so the material has time to respond fully to each change in the field direction. As the frequency increases, the period of the applied electric field becomes shorter than the relaxation time, so the material cannot respond fully to each change in the field direction [44].

3.5 Surface morphology of slabs

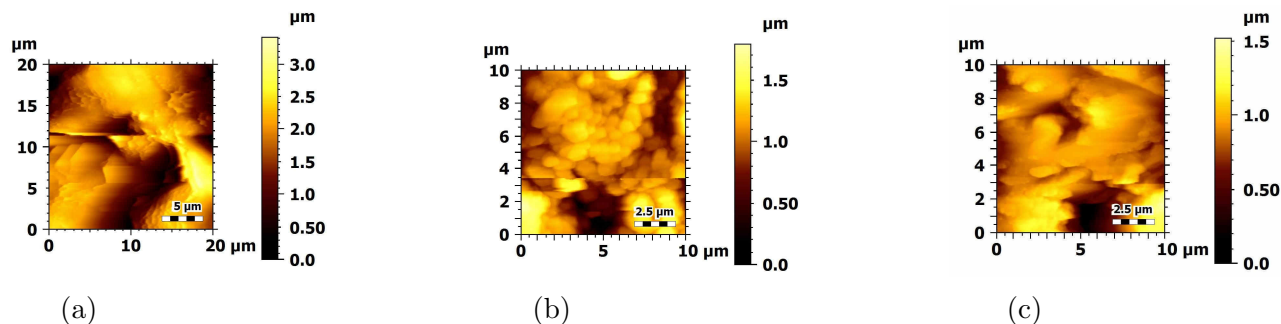


Figure 3.18: Surface of well polished slabs under AFM. The roughness of the respective area is given in the bracket (a) BaM (585 nm) (b) BaY (266 nm) (c) PbM (194 nm)

3.6 Spin Seebeck Measurements

As of now, most of the research on Spin Seebeck Effect is being carried out on a class of compounds called garnets, especially YIG. Experiments have revealed that there appears to be a positive correlation between the SSE signal and the saturation magnetization of the material[56]. The saturation magnetization of YIG is reported to be 27.6 emu/g [23] and for the Y type hexaferrite $\text{Ba}_2\text{Zn}_2\text{Fe}_{12}\text{O}_{22}$, it was reported to be 42 emu/g [23]. Spin Seebeck measurements were already reported on thin films of $\text{BaFe}_{12}\text{O}_{19}$ [34] and $\text{Ba}_2\text{Zn}_2\text{Fe}_{12}\text{O}_{22}$ [23] but not on their bulk samples. There were no measurements reported for the lead substituted hexaferrites, either on thin film or bulk samples. So the motivation was to investigate the possibility of using hexaferrite as a potential spintronic material.

The temperature dependent measurement of SSE signal was carried out by cooling the sample from 298 K to 12 K and measuring the corresponding signal in step size 3 K, all while a field of 1990 Oe applied across the sample. A thermal gradient of 22 K was applied perpendicular to the magnetic field. To subtract the background signal, the magnetic field of 1990 Oe is applied in opposite polarity and the corresponding signals are subtracted and divided by two to obtain the absolute signal strength.

The field dependence of Spin Seebeck signal was carried out at 268 K for BaM and 210 K for PbM, with a maximum field of 1990 Oe, with the field applied in opposite directions to study the hysteresis. The signal increased with increase in magnetic field. As the magnetic field required to saturate the magnetization is beyond the range of our apparatus, the SSE signal could not be brought to saturation.

The temperature gradient dependence of Spin Seebeck signal was carried out at a magnetic field of 1990 Oe. The sample temperature was maintained at 258 K, while the temperature gradient across the sample was raised from 2 K to 22 K in step size of 2 K. There appears to be a linear relationship between the temperature gradient and the signal. This shows that there is no thermal loss.

3.6.1 PbM

Platinum was deposited over the entire surface of the slab using sputtering. Its thickness was measured to be 30 nm, distance between contacts 4.50 mm and width of 2.11 mm. The thickness of the slab was measured to be 0.41 mm.

Spin Seebeck signal was measured on the sample and the measured data was normalized by the equation

$$V_{LSSE} = \frac{V_{obs}t}{\Delta T R_{pt}l} \quad (3.1)$$

where V_{obs} is the observed potential difference across the platinum, t is the thickness of the slab, ΔT is the temperature difference applied across the slab, R_{pt} is the resistance of the platinum bar at the measurement temperature and l is the distance between the contacts on the platinum layer.

The data after normalization is as given below

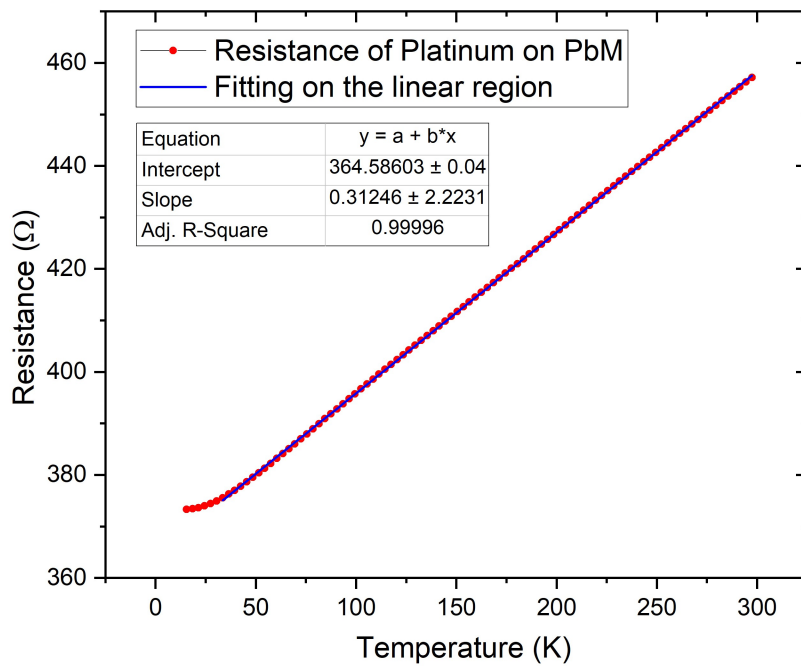


Figure 3.19: Resistance of platinum deposited on top as a function of temperature

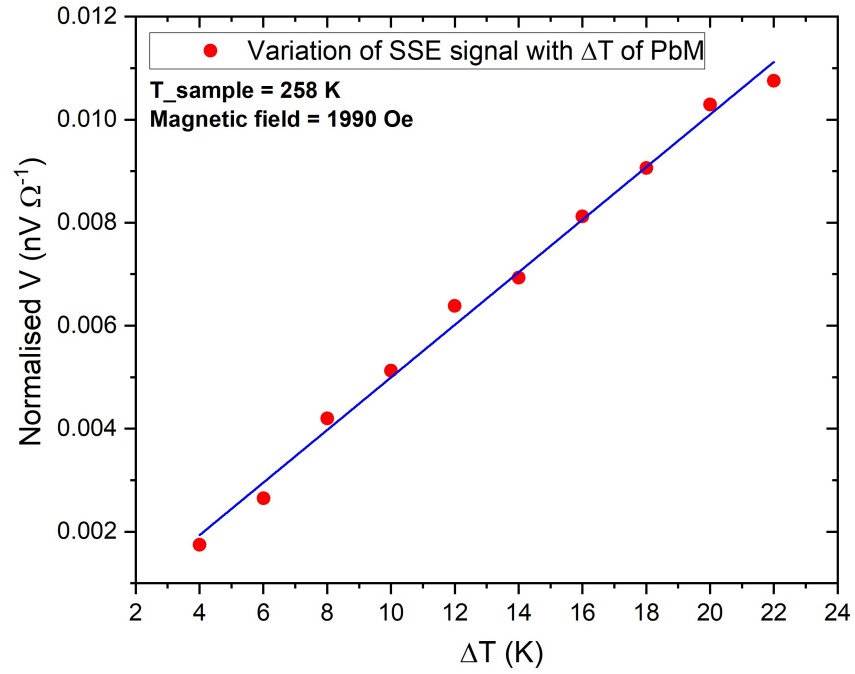


Figure 3.20: Spin Seebeck signal as a function of thermal gradient

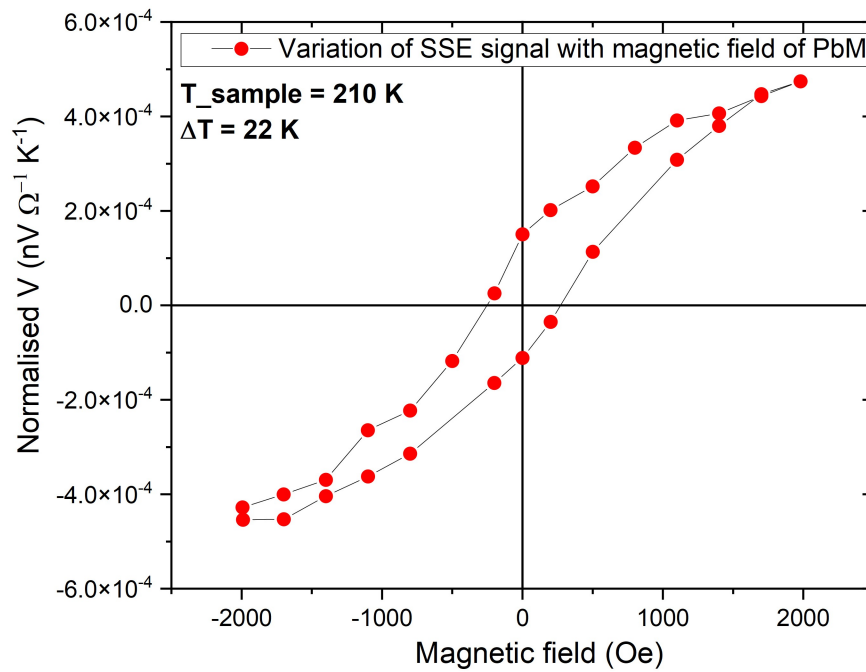


Figure 3.21: Spin Seebeck signal as a function of magnetic field

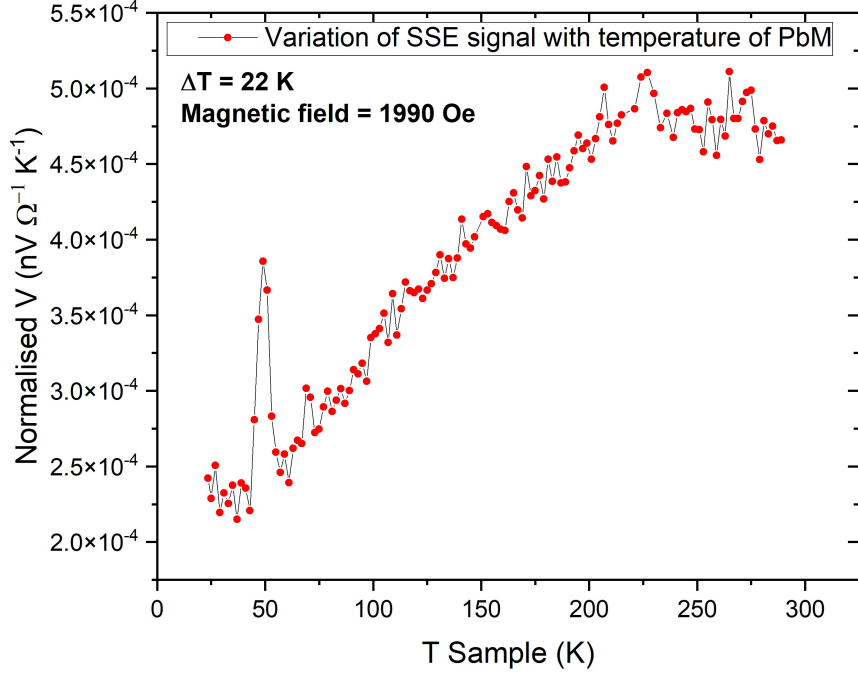


Figure 3.22: Spin Seebeck signal as a function of temperature

3.6.2 BaM

Platinum was deposited over the entire surface of the slab using sputtering. Its thickness was measured to be 30 nm, the distance between contacts 4.44 and width of 2.14 mm. The thickness of the slab was measured to be 0.45 mm.

Spin Seebeck signal was measured on the sample and the measured data was normalized by the equation

$$V_{LSSE} = \frac{V_{obs}t}{\Delta T R_{pt}l} \quad (3.2)$$

where V_{obs} is the observed potential difference across the platinum, t is the thickness of the slab, ΔT is the temperature difference applied across the slab, R_{pt} is the resistance of the platinum bar at the measurement temperature and l is the distance between the contacts on the platinum layer.

The data after normalization is as given below

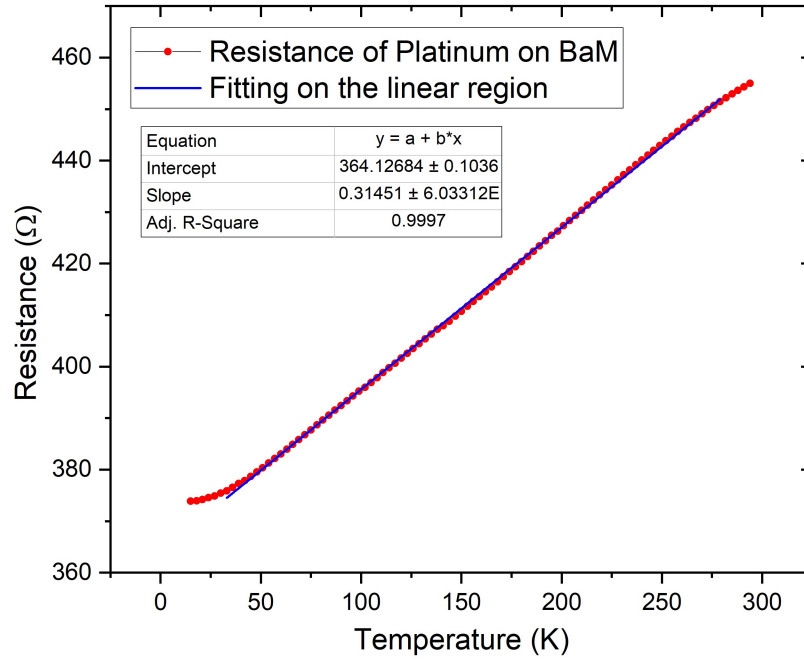


Figure 3.23: Resistance of platinum deposited on top as a function of temperature

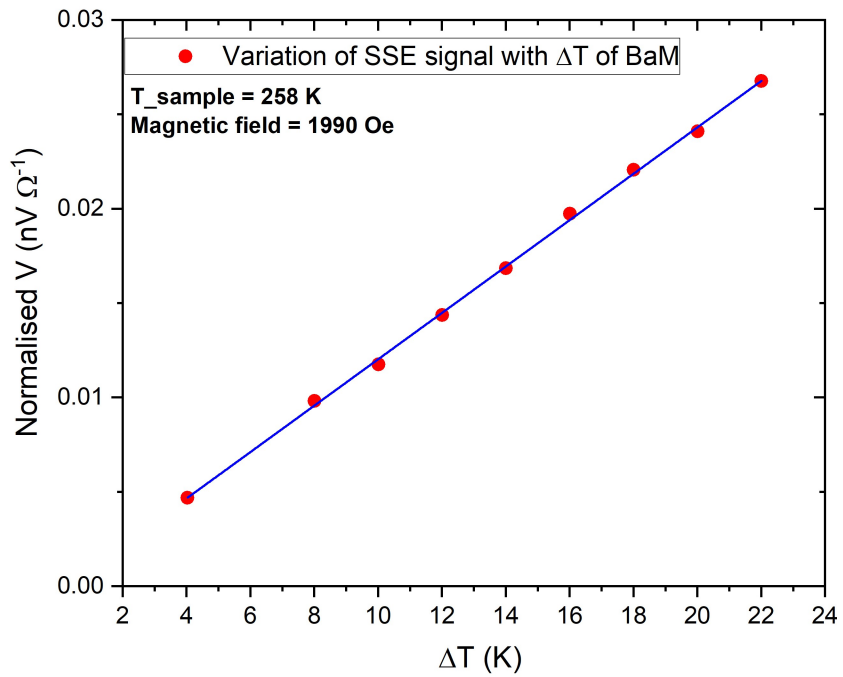


Figure 3.24: Spin Seebeck signal as a function of thermal gradient

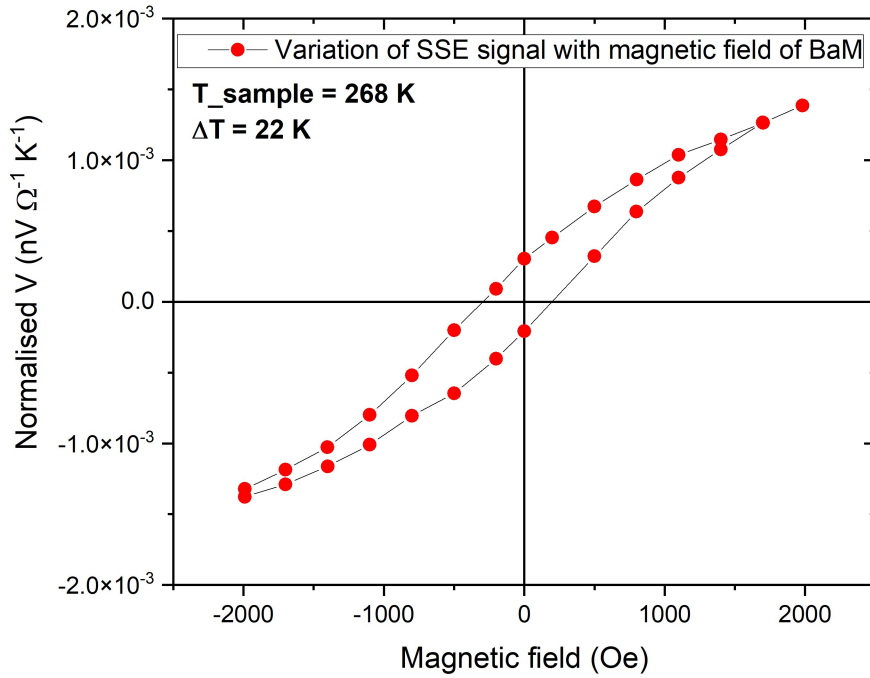


Figure 3.25: Spin Seebeck signal as a function of magnetic field

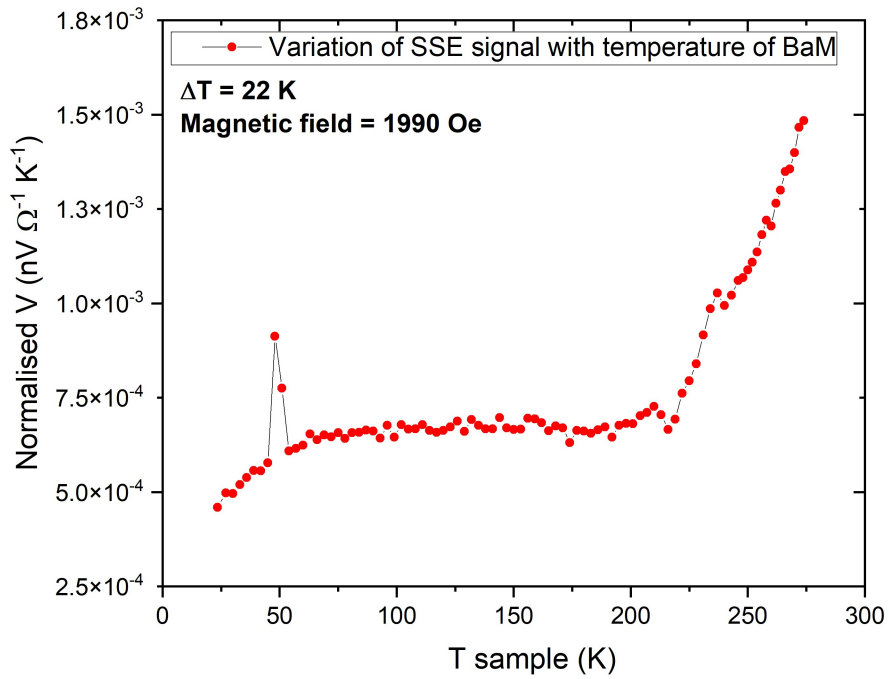


Figure 3.26: Spin Seebeck signal as a function of temperature

As we can see from the graphs 3.19 and 3.23, the resistance of platinum on top varies linearly with temperature as expected of a metal behaviour. Least square fitting was done on the observed data to obtain the linear equation which was used to normalize the subsequent data obtained.

From the graphs 3.20 and 3.24, it was observed that the SSE signal varies linearly with the temperature as expected from the equation 1.8. This also shows that there is no thermal loss.

Graphs 3.21 and 3.25 shows the variation of the SSE signal with magnetic field. The observed data reflects the dependence of the signal on the magnetization of the sample. Despite the absence of a magnetic field, a signal is still present due to the remanent magnetic field, as can be observed. The sign of the signal also flips when polarity of the field is reversed.

Graphs 3.22 and 3.26 shows the variation of SSE signal with temperature for PbM. The signal decreases as the temperature decreases. To identify the exact cause for the reduction in signal, a detailed analysis is required. It may be attributed to the decrease in magnon population with lowering of temperature [18]. It was also noticed that the signal from BaM is slightly higher than that from PbM. There also appears to be a sudden increase in the signal from BaM above 225 K. This is suspected to originate from the Anomalous Nernst Effect contribution caused by the low resistivity of the sample. Further measurements are required to confirm any contributions from ANE.

In the case of BaY, no Spin Seebeck voltage was measured on the sample. In depth investigation is required to find the exact cause of absence of the signal.

Chapter 4

Conclusion and future works

In summary, samples of $\text{PbFe}_{12}\text{O}_{19}$, $\text{Ba}_2\text{Zn}_2\text{Fe}_{12}\text{O}_{22}$, $\text{BaFe}_{12}\text{O}_{19}$ were synthesised via solid state synthesis. Characterization techniques of XRD, FE SEM and EDX confirmed the purity of the samples. Structural analysis using Rietveld was performed with good fits and lattice parameters were obtained. Additional measurements like resistivity and dielectric measurements were also carried out. Spin Seebeck measurements were carried out in the three samples. While the samples $\text{PbFe}_{12}\text{O}_{19}$ and $\text{BaFe}_{12}\text{O}_{19}$ gave Spin Seebeck signal, $\text{Ba}_2\text{Zn}_2\text{Fe}_{12}\text{O}_{22}$ produced no signal. A slight difference in signal strength was noted between $\text{BaFe}_{12}\text{O}_{19}$ and $\text{PbFe}_{12}\text{O}_{19}$, with the former exhibiting a slightly higher signal.

Future plans of the project include checking for any Anomalous Nernst Effect contributions to the signal by coating with copper instead of platinum. Future plans also include synthesising $\text{Pb}_2\text{Zn}_2\text{Fe}_{12}\text{O}_{22}$ via co precipitation method and its characterization. Also planned is the synthesis and characterization of $\text{Pb}_3\text{Zn}_2\text{Fe}_{24}\text{O}_{41}$. Additionally, fabrication of thin films of all the samples using either spin coating or Pulse Laser Deposition, followed by measurement of the Spin Seebeck effect on them is also planned.

Bibliography

- [1] Hiroto Adachi et al. “Theory of the spin Seebeck effect”. In: *Reports on Progress in Physics* 76.3 (2013), p. 036501.
- [2] *AdNaNo*. <https://www.adnano-tek.com/magnetron-sputtering-deposition-msd.html>.
- [3] Neil W Ashcroft and N David Mermin. *Solid State Physics*. Holt, Rinehart and Winston, 1976.
- [4] Neil W Ashcroft and N David Mermin. *Solid state physics*. Cengage Learning, 2022.
- [5] Wilhelm Heinrich von AULOCK et al. *Handbook of Microwave Ferrite Materials*. Edited by Wilhelm H. Von Aulock. Contributors: Arnold S. Boher. John F. Ollom, Robert F. Rauchmiller. Academic Press, 1965.
- [6] Yang Bai et al. “Preparation and magnetic characterization of Y-type hexaferrites containing zinc, cobalt and copper”. In: *Materials Science and Engineering: B* 99.1-3 (2003), pp. 266–269.
- [7] Mario Norberto Baibich et al. “Giant magnetoresistance of (001) Fe/(001) Cr magnetic superlattices”. In: *Physical review letters* 61.21 (1988), p. 2472.
- [8] Y Ben Taher et al. “Conductivity study and correlated barrier hopping (CBH) conduction mechanism in diphosphate compound”. In: *Applied Physics A* 120 (2015), pp. 1537–1543.
- [9] Gerd Binnig, Calvin F Quate, and Ch Gerber. “Atomic force microscope”. In: *Physical review letters* 56.9 (1986), p. 930.
- [10] Arnab Bose and Ashwin A Tulapurkar. “Recent advances in the spin Nernst effect”. In: *Journal of Magnetism and Magnetic Materials* 491 (2019), p. 165526.

- [11] CHEMEUROPE. <https://www.chemeurope.com/en/news/163870/smooth-propagation-of-spin-waves-using-gold.html>.
- [12] Anil Prabhakar Daniel D. Stancil. *Spin Waves Theory and Application*. Springer, 2009.
- [13] Cihangir Duran, Susan Trolier-McKinstry, and Gary L Messing. “Processing and electrical properties of 0.5 Pb (Yb 1/2 Nb 1/2) O 3-0.5 PbTiO 3 ceramics”. In: *Journal of electroceramics* 10 (2003), pp. 47–55.
- [14] Mikhail I Dyakonov and VI Perel. “Current-induced spin orientation of electrons in semiconductors”. In: *Physics Letters A* 35.6 (1971), pp. 459–460.
- [15] Yuan Ping Feng et al. “Prospects of spintronics based on 2D materials”. In: *Wiley Interdisciplinary Reviews: Computational Molecular Science* 7.5 (2017), e1313.
- [16] Roland A Fleck and Bruno M Humbel. *Biological Field Emission Scanning Electron Microscopy, 2 Volume Set*. John Wiley & Sons, 2019.
- [17] Mahdieh Ghaseminejad, Leila Gholamzadeh, and Fatemeh Ostovari. “Investigation of x-ray attenuation property of modification PbO with graphene in epoxy polymer”. In: *Materials Research Express* 8.3 (2021), p. 035008.
- [18] Er-Jia Guo et al. “Influence of thickness and interface on the low-temperature enhancement of the spin Seebeck effect in YIG films”. In: *Physical Review X* 6.3 (2016), p. 031012.
- [19] Koichi Haneda, Choji Miyakawa, and Hiroshi Kojima. “Preparation of High-Coercivity BaFe₁₂O₁₉”. In: *Journal of the American Ceramic Society* 57.8 (1974), pp. 354–357.
- [20] M Zahid Hasan and Charles L Kane. “Colloquium: topological insulators”. In: *Reviews of modern physics* 82.4 (2010), p. 3045.
- [21] Atsufumi Hirohata and Koki Takanashi. “Future perspectives for spintronic devices”. In: *Journal of Physics D: Applied Physics* 47.19 (2014), p. 193001.
- [22] JE Hirsch. “Spin hall effect”. In: *Physical review letters* 83.9 (1999), p. 1834.
- [23] J Hirschner et al. “Spin Seebeck effect in Y-type hexagonal ferrite thin films”. In: *Physical Review B* 96.6 (2017), p. 064428.
- [24] Axel Hoffmann. “Spin Hall effects in metals”. In: *IEEE transactions on magnetics* 49.10 (2013), pp. 5172–5193.

- [25] Friso Jacobus Jedema, AT Filip, and BJ Van Wees. “Electrical spin injection and accumulation at room temperature in an all-metal mesoscopic spin valve”. In: *Nature* 410.6826 (2001), pp. 345–348.
- [26] JM Juneja and TK Mukherjee. “A study of the purification of metallurgical grade silicon”. In: *Hydrometallurgy* 16.1 (1986), pp. 69–75.
- [27] P Kameli et al. “Structure and Magnetization of Strontium Hexaferrite (SrFe₁₂O₁₉) Films Prepared by Pulsed Laser Deposition”. In: *Frontiers in Materials* (2021), p. 365.
- [28] Safa O Kasap. *Electronic materials and Devices*. McGraw-Hill New York, 2006.
- [29] Peter J Kelly and R Derek Arnell. “Magnetron sputtering: a review of recent developments and applications”. In: *Vacuum* 56.3 (2000), pp. 159–172.
- [30] Manabu Kiguchi. *Compendium of Surface and Interface Analysis*. Springer, 2018.
- [31] Takashi Kikkawa and Eiji Saitoh. “Spin Seebeck effect: Sensitive probe for elementary excitation, spin correlation, transport, magnetic order, and domains in solids”. In: *Annual Review of Condensed Matter Physics* 14 (2023), pp. 129–151.
- [32] Dietmar Kobertz. “Vaporization and caloric studies on yellow lead oxide PbO”. In: *Calphad* 65 (2019), pp. 155–164.
- [33] Karel Kouril. “Local structure of hexagonal ferrites studied by NMR”. PhD thesis. 2013.
- [34] Peng Li et al. “Generation of pure spin currents via spin Seebeck effect in self-biased hexagonal ferrite thin films”. In: *Applied Physics Letters* 105.24 (2014), p. 242412.
- [35] Darja Lisjak and Miha Drogenik. “The low-temperature formation of barium hexaferrites”. In: *Journal of the European Ceramic Society* 26.16 (2006), pp. 3681–3686.
- [36] Y Marouani et al. “Electrical conductivity and dielectric properties of Sr doped M-type barium hexaferrite BaFe₁₂O₁₉”. In: *RSC advances* 11.3 (2021), pp. 1531–1542.
- [37] Yazan Maswadeh. “STRUCTURAL ANALYSIS OF HEXAFERRITE MATERIALS”. PhD thesis. Aug. 2014.
- [38] Takashi Nagatani et al. “Development of an ultra high resolution scanning electron microscope by means of a field emission source and in-lens system”. In: *Scanning Microscopy* 1.3 (1987), p. 3.

- [39] X Obradors et al. “X-ray analysis of the structural and dynamic properties of BaFe₁₂O₁₉ hexagonal ferrite at room temperature”. In: *Journal of Solid State Chemistry* 56.2 (1985), pp. 171–181.
- [40] S Prathap, W Madhuri, and Sher Singh Meena. “Multiferroic properties and Mössbauer Study of M-type hexaferrite PbFe₁₂O₁₉ synthesized by the high energy ball milling”. In: *Materials Characterization* 177 (2021), p. 111168.
- [41] *PubChem*. <https://pubchem.ncbi.nlm.nih.gov/compound/Lead-monoxide#section=Melting-Point>.
- [42] *PubChem*. <https://pubchem.ncbi.nlm.nih.gov/compound/Lead-monoxide#section=Boiling-Point>.
- [43] Robert C Pullar. “Hexagonal ferrites: a review of the synthesis, properties and applications of hexaferrite ceramics”. In: *Progress in Materials Science* 57.7 (2012), pp. 1191–1334.
- [44] Ch Rayssi et al. “Frequency and temperature-dependence of dielectric permittivity and electric modulus studies of the solid solution Ca_{0.85}Er_{0.1}Ti_{1-x}Co_{4x/3}O₃ (0 < x < 0.1)”. In: *Rsc Advances* 8.31 (2018), pp. 17139–17150.
- [45] Nur Ain Nabilah Razali et al. “Physical and Shielding Protection Parameterization of PbO-ZnO-B₂O₃-SiO₂ Glass Network”. In: *Journal of Physics: Conference Series*. Vol. 1083. 1. IOP Publishing, 2018, p. 012005.
- [46] SM Rezende et al. “Magnon spin-current theory for the longitudinal spin-Seebeck effect”. In: *Physical Review B* 89.1 (2014), p. 014416.
- [47] David W Richerson and William E Lee. *Modern ceramic engineering: properties, processing, and use in design*. CRC press, 2018.
- [48] Junren Shi et al. “Proper definition of spin current in spin-orbit coupled systems”. In: *Physical review letters* 96.7 (2006), p. 076604.
- [49] HS Shin and S-J Kwon. “X-ray powder diffraction patterns of two Y-type hexagonal ferrites”. In: *Powder Diffraction* 8.2 (1993), pp. 98–101.
- [50] L Simon-Seveyrat et al. “Re-investigation of synthesis of BaTiO₃ by conventional solid-state reaction and oxalate coprecipitation route for piezoelectric applications”. In: *Ceramics international* 33.1 (2007), pp. 35–40.

- [51] Virender Pratap Singh et al. “A current review on the synthesis and magnetic properties of M-type hexaferrites material”. In: *World Journal of Condensed Matter Physics* 8.02 (2018), p. 36.
- [52] Jairo Sinova et al. “Spin hall effects”. In: *Reviews of modern physics* 87.4 (2015), p. 1213.
- [53] Andreas Stein, Steven W Keller, and Thomas E Mallouk. “Turning down the heat: Design and mechanism in solid-state synthesis”. In: *Science* 259.5101 (1993), pp. 1558–1564.
- [54] Mark D Stiles and A Zangwill. “Anatomy of spin-transfer torque”. In: *Physical Review B* 66.1 (2002), p. 014407.
- [55] Brian H Toby. “R factors in Rietveld analysis: How good is good enough?” In: *Powder diffraction* 21.1 (2006), pp. 67–70.
- [56] K Uchida et al. “Longitudinal spin Seebeck effect in various garnet ferrites”. In: *Physical Review B* 87.10 (2013), p. 104412.
- [57] K Uchida et al. “Observation of the spin Seebeck effect”. In: *Nature* 455.7214 (2008), pp. 778–781.
- [58] K Uchida et al. “Thermal spin pumping and magnon-phonon-mediated spin-Seebeck effect”. In: *Journal of Applied Physics* 111.10 (2012), p. 103903.
- [59] Ken-ichi Uchida et al. “Spin seebeck insulator”. In: *Nature materials* 9.11 (2010), pp. 894–897.
- [60] John G Webster. *Electrical measurement, signal processing, and displays*. CRC Press, 2003.
- [61] Anthony R West. *Solid state chemistry and its applications*. Wiley, 2014.
- [62] *Wikipedia*. https://en.wikipedia.org/wiki/Atomic_force_microscopy.
- [63] *X-ray diffraction (XRD)*. <https://wiki.anton-paar.com/se-en/x-ray-diffraction-xrd/>.
- [64] Jiang Xiao et al. “Theory of magnon-driven spin Seebeck effect”. In: *Physical Review B* 81.21 (2010), p. 214418.

- [65] Ke Yang et al. “Fluoro-polymer@ BaTiO₃ hybrid nanoparticles prepared via RAFT polymerization: toward ferroelectric polymer nanocomposites with high dielectric constant and low dielectric loss for energy storage application”. In: *Chemistry of Materials* 25.11 (2013), pp. 2327–2338.
- [66] Robert Alan Young. *The Rietveld Method. International union of Crystallography.* 1993.
- [67] S Yuasa and DD Djayaprawira. “Giant tunnel magnetoresistance in magnetic tunnel junctions with a crystalline MgO (0 0 1) barrier”. In: *Journal of Physics D: Applied Physics* 40.21 (2007), R337.